Design, Fabrication and Characterization of a Microfluidic Device for Ultrasound-based Cell Sorting

Pratik Anirudha Ambekar

A thesis

submitted in partial fulfillment of the

requirements for the degree of

Master of Science in Mechanical Engineering

University of Washington

2021

Committee:

Thomas Matula

Oleg Sapozhnikov

Michael Bailey

Nathan Sniadecki

Program Authorized to Offer Degree:

Mechanical Engineering

University of Washington

Abstract

Design, Fabrication and Characterization of a Microfluidic Device for Ultrasound-based Cell Sorting

Pratik Anirudha Ambekar

Chair of the supervisory committee:

Dr. Thomas Matula

Department of Bioengineering

The isolation and sorting of cells is an important process in research and hospital laboratories. Most research laboratories incorporate fluorescently or magnetically labeled antibodies adherent to cell surface antigens for cell identification and separation. MiCS (Microbubble Cell Sorting) is a new technique that overcomes the limitations of existing cell sorting techniques by using ultrasound traveling waves and microbubble tags. A microfluidic device consisting of a flow channel was developed for effectively performing MiCS. The device was designed with the aim of obtaining traveling waves in the flow channel by using various design considerations and Finite Element Analysis (FEA) simulations. Placing the flow channel in the acoustic far-field provided the necessary traveling-wave regime. Subsequently, the device was fabricated by employing manufacturing processes like laser cutting, micromachining, and acrylic bonding. The device was then characterized by performing electrical impedance analysis, flow continuity experiments, and pulse-echo testing. Results suggested that flow in the flow channel was continuous, and the transducer operated effectively.

Table of Contents

List of Figures

List of Tables

ACKNOWLEDGEMENTS

I would like to express my sincere gratitude to my advisor, Dr. Thomas Matula for giving me an opportunity to contribute to this research and work under his guidance. I would also like to express my deepest gratitude to Dr. Oleg Sapozhnikov for guiding me throughout this project.

I would like to thank Dr. Mike Bailey and Dr. Nathan Sniadecki for being on my thesis committee and giving valuable guidance. Special thanks to Katy Kuznetsova and Elizabeth Lynch for teaching me various machining processes and helping me in fabrication. I would like to thank Brian MacConaghy, Dr. Mohamed Ghanem, Dr. Randall Williams, Dr. Alex Peek and Dr. Adam Maxwell for their continued support and interest in the project. A special thanks to my lab mates Yashwanth NandaKumar and Minho Song for their help and advice during my research work.

Finally, I would like to acknowledge the support and encouragement from my family, friends and teachers.

DEDICATION

To my parents

Chapter 1. Introduction

1.1) Significance

Cell sorting is the isolation of one or more cell types from a heterogeneous cell population which is essential to modern biological research and clinical diagnosis. Understanding cell behavior requires homogenous cell populations. Cell sorting technologies underpin many discoveries in cell biology. Induced pluripotent stem cells derived from fibroblasts, have bypassed the moral and political issues regarding research with embryonic stem cells [1, 2]. Treatments and management of HIV-infected white blood cells have benefited from advanced cell sorting techniques [3, 4]. In oncology, cell-separation techniques are routinely used to separate cells for diagnostic purposes. In addition to this, cell sorting is required in fields like genomics and proteomics which require precise control of cell populations [5-8]. Samples of interest often contain heterogeneous cell populations. Hence it is critical to isolate specific cells for understanding their function and how they respond to various stimuli. Cell sorting also is essential for tissue engineering and regenerative medicine. Strategies require that stem and progenitor cells be isolated from their native environments.

1.2) Cell separation techniques

There are various cell sorting techniques [9, 10], and each has advantages and disadvantages and is utilized in specific conditions. New methods are being developed to handle specialized needs. Antibody labeling techniques have better sensitivity and specificity than bulk cell separation techniques, and hence, are widely used [9]. Cell sorting is mostly performed with developed technologies such as fluorescence-based or magnetic based systems.

1.3) Fluorescently Activated Cell Sorting (FACS)

Fluorescently Activated Cell Sorting (FACS) was developed in the 1960s and has been continuously improved thereafter[11, 12]. This technique can be considered as the benchmark for the development of other cell sorting techniques. The technique uses a flow cytometer with additional fluorescence lasers and fluorescent particles adhered to cell surface proteins to identify cells of interest for downstream sorting. A key advantage of FACS is that it can sort against several markers. One can use several fluorophores that emit in different wavelengths to sort a cell based on a combination of fluorescent emissions and hence, a combination of surface protein expressions. However, FACS is often too complex and expensive for individual laboratories. Therefore it is outsourced to core facilities where highly trained technicians continuously align and fine-tune sheath flow rates, sample flow rates, gain and discrimination settings for each sample run.

1.4) Magnetically Activated Cell Sorting (MACS)

A new technique was developed in 1989 at the Univ. of Cologne by Stefan Miltenyi that replaced the fluorophores with magnetic particles and used magnetic fields to isolate the conjugated cells. The technique is called Magnetically Activated Cell Sorting (MACS) [13]. This technique is very powerful because it is simple and inexpensive to use, making it widely available to most researchers. Also, the manufacture and sale of magnetic particles for MACS instruments has become a specialized field on its own, with several major suppliers, just as fluorescent particles are for FACS instruments.

However, MACS also has drawbacks that motivate the development of other technologies. Commercial MACS systems significantly only sort against a single marker because all magnetic

particles interact similarly with the magnetic field. To sort against multiple markers, one has to process the samples serially. This is both time-consuming and is fraught with difficulties. Many research groups attempted multitarget magnetic separation by applying various techniques such as the use of dipoles [14], traveling wave magnetophoresis [15], free-flow magnetophoresis [16, 17], external magnetics strips [18], or microchannel-embedded staggered magnetic strips [19]. In some of these cases, microfluidic technologies were used to control the fluidic and magnetophoretic forces that govern separation performance parameters like purity, recovery and throughput. Although somewhat promising, the previously mentioned technologies have not demonstrated high-purity, multitarget magnetic sorting with high throughput. This limitation can be overcome by leveraging the resonance response of microbubbles, allowing one to affect a specific size using an appropriate driving frequency.

1.5) Microfluidic cell sorting

Though FACS and MACS are the two leading commercial cell sorting techniques, new techniques are being developed. There are several groups using standing acoustic waves to separate particles and cells [20-36]. The principle for these techniques were first established by Coakley, et al., [37, 38]. A potential advantage of these systems is that separation can be label-free. But label-free acoustophoretic techniques require a significant difference in morphology, density, or compressibility between the particles to efficiently separate them. Cells can be separated from particles, but not from other similar cells. All label-free acoustic separation techniques align the cells at the pressure node, as cells are positive contrast particles. One group developed negative acoustic contrast elastomeric particles that when adhered to the cells, forces cells to the pressure antinode instead of the node [22, 36]. These particles cannot be manipulated further since they are not resonant.

It is difficult to sort subpopulations of cells from other cells using only ultrasound, as cells of similar size all respond nearly the same. As discussed above, by itself, ultrasound can only sort objects that are much different in morphology, density or compressibility. To overcome this limitation, cells expressing a particular antigen can be tagged with a marker that responds to ultrasound. An ideal marker will have a much stronger interaction with ultrasound than the cell.

There exist two techniques that use conjugate microbubbles to separate cells. One uses the buoyancy of microbubbles to separate conjugated vs unconjugated cells [39]. With buoyancy-activated cell sorting, all cells conjugated to microbubbles rise to the surface where the cells are manually collected from the top. The two major drawbacks of this technology are low throughput and single marker sorting. Another microbubble-conjugation technique uses a standing wave lab-on-a-chip similar to the elastomeric particles [23], but cannot take advantage of microbubble resonances to sort against multiple markers, because different frequencies require different geometries.

In order to overcome the limitations of the techniques mentioned above, Microbubble Cell Sorting (MiCS) technique was introduced [40]. It consists of conjugated microbubbles and ultrasound traveling waves to separate cells. Figure 1 shows the principle of MiCS. When compared to other microfluidic systems, it overcomes the geometrical limitations of standing wave systems that can only use specific frequencies. It also overcomes spatial limitations of separating particles a maximum of a half-wavelength. The advantages of FACS like the ability to sort against multiple markers are retained in MiCS while the disadvantages of FACS like high cost and complicated usage are eliminated. MiCS also eliminates some disadvantages of MACS, like ability to sort against only one target.

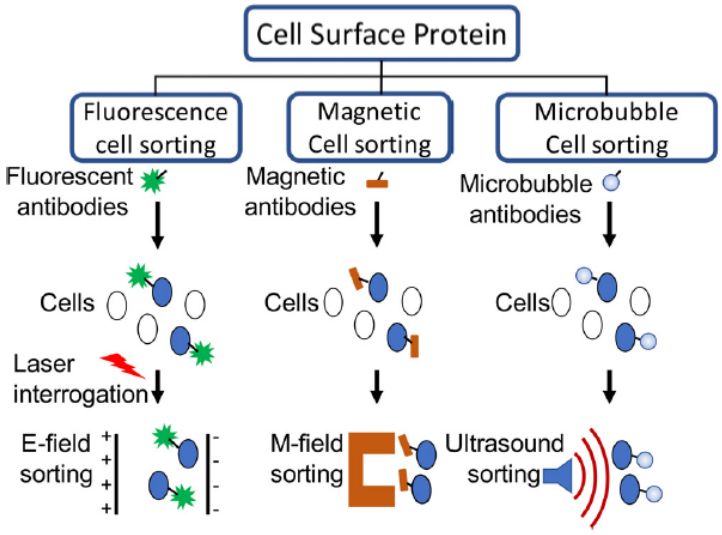

Figure 1. Cell purification methods based on cell surface antigen [3]

1.6) Scope of the thesis

The response of a cell-microbubble (MB) pair to an ultrasound pulse and their displacement relative to untagged cells was studied and the feasibility of MiCS was proved [40]. The next step was to develop a device capable of executing MiCS process. Few devices were developed by employing an experimental approach, which failed to create traveling waves in the flow channel. Finite Element Analysis (FEA) modeling was needed to analyze acoustic variables in the device. The objectives of this thesis were threefold. The first objective was to design the device by applying various design parameters and optimizing the dimensions by performing FEA simulations. The second objective was fabricating the device by using suitable manufacturing processes. The third objective consisted of characterizing the fabricated device to ensure its suitability for testing.

Chapter 2. Design

A sample Computer-Aided Design (CAD) model of the microfluidic device was constructed (figure 2) with arbitrary dimensions subject to modifications. The transducer (ABCD) was responsible for introducing ultrasonic waves in the acrylic cutouts. Acrylic cutouts (EFGHI) that were cut from acrylic sheets were used as a medium for wave transmission. The cell sorting process was supported by a two-port input-output flow chamber (IJKL) machined inside the acrylic cutouts. A triangular section (FGH) was introduced to eliminate reflections back towards the flow channel and a square section (IE) was cut to accommodate the transducer.

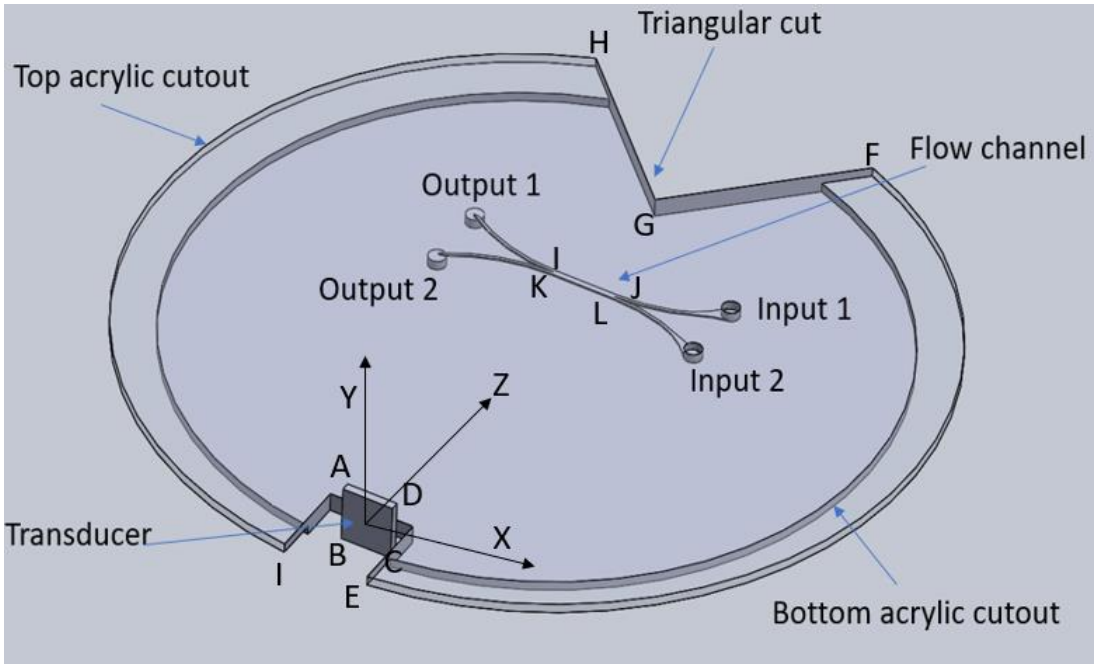

Figure 2. One of the possible designs of the cell sorting device

2.1) Hypothesized cell sorting process

Consider a blood sample containing Leukemia cells tagged by microbubbles. We hypothesized that the cell sorting process that consists of separating tagged Leukemia cells (cell-microbubble conjugates) from the blood sample would take place as follows.

Blood solution will be injected in the device through input port 2 and a sheath solution (water or saline) will be injected simultaneously through input port 1 figure (2) at specific flow rates. The flow rate of both solutions will be adjusted to ensure that the flow is laminar. As mentioned in ref [59], when two or more streams with low Re are joined into a single stream, also with low Re, by using a junction of appropriate connectivity, the combined streams flow parallel to each other without turbulent mixing. Hence, the two solutions do not under-go turbulent mixing due to which the cell-microbubble conjugates in the blood sample flow do not cross the boundary between sheath flow and blood sample flow unless an acoustic force is applied. A transducer coupled to the acrylic cutouts is responsible for application of the acoustic radiation force, a force which acts on the microbubbles [40]. Once the transducer is activated, a pressure field is formed in the cutouts due to which pressure variations are created in the flow channel [58]. The dimensions in the flow channel will be optimized so that these pressure variations create a traveling wave in z-direction in the flow channel. The cell-microbubble conjugates translate under the influence of traveling waves [40] and cross the laminar flow boundary reaching sheath flow. Note that the effect of acoustic radiation force is much more on microbubbles than the cells. Still, since the cells are conjugated to microbubbles, the cells translate along with the microbubbles. The sheath flow now containing cell-microbubble conjugates will be collected at output 1, whereas the blood sample will be collected at output 2. Microbubbles will be removed by applying a small over pressure. Thus, a sheath solution consisting of Leukemia cells will be obtained at output 1. This process will be visualized with the help of a microscope that will be focused on the flow channel to ensure that the acoustic field is indeed acting on the cell-microbubble conjugates.

It was necessary to optimize the dimensions of the device in order to ensure traveling waves in the flow channel. The dimensions and materials of each component of the device were finalized based on various design considerations. The design process is explained in the following sections.

2.2) Acrylic cutouts

For the device, we considered acrylic, PDMS, silicon, glass and polycarbonate as possible material choices. Acrylic was chosen because of low cost, ease of micromachining, optical transparency.

A circular shape was selected because of the constraints associated with mounting the apparatus in the inverted microscope. The diameter of the circular opening of the mounting apparatus was 80 mm. Hence, to fit the device in the provided space, the diameter of the lower cutout (shown in figure 1) was 80 mm. The upper cutout (figure 1) was also circular in shape for keeping consistency. The diameter of the upper cutout was 90 mm so that the device will rest on a ledge of the mounting apparatus. The thickness of both cutouts was determined to be 1 mm each, to curtail the formation of Lamb modes. A triangular section (FGH in figure 2) was cut for eliminating acoustic reflections back towards the flow channel. A square section (IE in figure 2) was cut for accommodating the transducer.

2.3) Flow channel

Figure 3 shows the flow channel as viewed from the top. (IJGF) was the central channel which supported the cell sorting process. Data from previous iterations of the device suggested that 10 mm length of the central channel was sufficient for occurrence and observation of the cell sorting process. Hence, the length of the central channel was finalized at 10 mm. The width (figure 3) of the central channel was optimized based on the microscope's field of view, which allowed for a maximum width of 0.7 mm. Hence, the width was finalized at 0.7 mm, although other values were

considered in the simulations for optimization. The height of the flow channel was optimized based on the microscope focusing capability of the lens, which allowed a maximum of 0.15 mm. Hence, the height was finalized at 0.15 mm, although other values were considered in the simulations for optimization. The radius of the inlet flow channel and outlet flow channel was determined as 20 mm based on the dimensions of the previous iterations of the device, which allowed for non-turbulent flow of the flow around the junctions (points B and C). The distance of the flow channel from the transducer was determined by performing FEA simulations. Figure 4 shows the optimized dimensions of the device, out of which some dimensions could be changed in the next section.

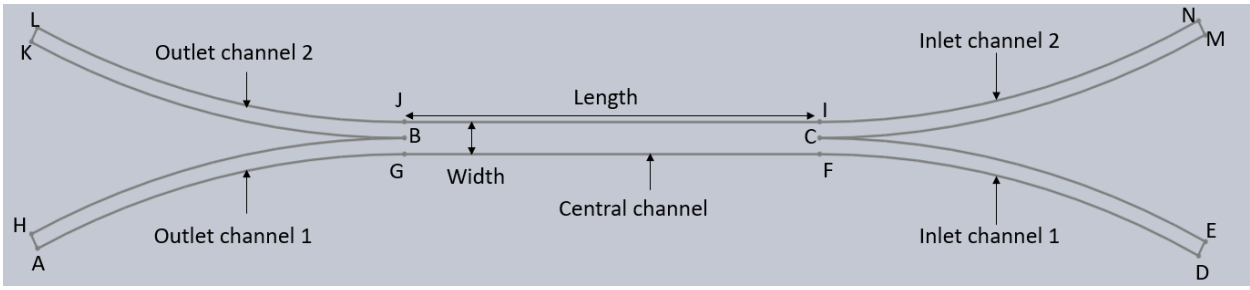

Figure 3. Top view of the flow channel

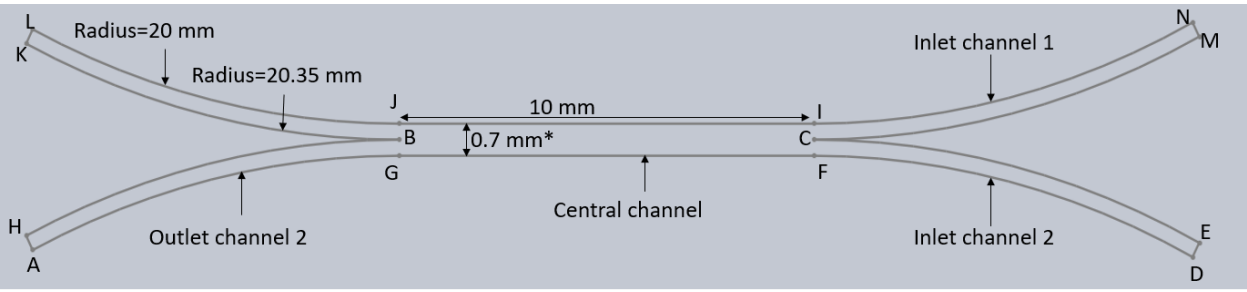

*Figure 4. Finalized dimensions of the flow channel. * denotes subject to change*

2.4) Transducer

PZT (Lead-Zirconate-Titanate) was selected as the material for the transducer due to its easy availability and experience of use. PZT-4 was selected due to its suitability for medium to high power applications. The height (figure 2 side AB) of the transducer was initially determined as 2

mm to coincide with the total length of the acrylic cutouts but was increased to 6 mm to provide space for soldering electrical connections. The width (figure 2 side BC) of the transducer was optimized based on FEA simulations.

2.4.1) Driving frequency of the transducer

The driving frequency was optimized based only on the microbubbles and not cell-microbubble conjugates for simplicity purposes. Microbubbles are sensitive to the frequency of the traveling ultrasound wave. Microbubble translation velocity is dependent on the driving frequency of the ultrasound wave as shown in equation 1. It was clear that the translation velocity was maximum when the driving frequency ω was equal to the resonance frequency. It was beneficial to have higher translational velocity since it would increase the sorting efficiency. Hence, the aim was to finalize the driving frequency close to the resonance frequency.

$$u = \frac{|P|^2}{3\eta\rho c\omega} \frac{\frac{1}{Q}}{[(1-\xi)]^2+\left(\frac{1}{Q}\right)^2} \quad (1)$$

Where,

P is the complex pressure amplitude of the wave (N/m^2).

η is the fluid viscosity ($N.s/m^2$).

ρ is the density of water (kg/m^2).

ω is the driving angular frequency (Hz).

$Q = \omega/2\delta$, is the bubble resonance quality factor, where δ is total damping constant.

$\xi = \omega_0/\omega$, where ω_0 is the resonance angular frequency.

Since driving the transducer close to the resonance frequency was required, a formula for obtaining the resonance frequency was needed. The resonance frequency of polydisperse microbubbles the radius of which ranged from 1 μm to 10 μm was calculated using equation 2 [45]. This formula incorporated coated microbubbles.

$$f_0 = \frac{1}{2\pi}\sqrt{\frac{1}{\rho R_0^2}\left[3\gamma P_0 + \frac{2(3\gamma-1)\sigma}{R_0} + \frac{4\chi}{R_0}\right]} \quad (2)$$

Where

$f_0 = \omega_0/2\pi$ is the resonance frequency (Hz).

ρ is the density of water, (1000 kg/m^3).

R_0 is the equilibrium radius of the oscillating bubble (m).

P_0 is the ambient pressure (10^5 Pa).

Υ is the polytropic exponent (1.07).

σ is the surface tension (0.072 N/m).

χ is the elasticity parameter (0.55 N/m).

The radius distribution ranged from 1 μm to 10 μm and corresponding frequency distribution was obtained using equation 2. We knew that the radius of most microbubbles was between 2 μm and 4 μm. The corresponding resonance frequency for 2 μm radius was 3.14 MHz whereas for 4 μm radius was 1.22 MHz as calculated from equation 2. Hence, to affect the maximum number of microbubbles, a frequency between 3.14 MHz and 1.22 MHz was required. 2 MHz transducers were readily available in our laboratory. Hence, the driving frequency was finalized at 2 MHz.

2.4.2) Thickness of the transducer

The thickness of the transducer is derived from the driving frequency by using equation 3.

$$f = c/2h \quad (3)$$

Where

f is the driving frequency.

c is the speed of sound in the transducer.

h is the thickness of the transducer.

Substituting the values c=4000 m/s for PZT-4 and f=2 MHz,

The thickness of the transducer was finalized at 1 mm.

In summary, a hypothesized cell sorting process subject to optimized dimensions of the device was explained. All dimensions except the width of the transducer and distance of the flow channel from the transducer were finalized. Dimensions like width and height of the flow channel were decided but could possibly be changed in case of undesirable results from simulations for those dimensions. The dimensions mentioned above would be finalized in the next chapter by performing frequency domain FEA simulations in COMSOL Multiphysics.

Chapter 3. Simulations in COMSOL Multiphysics

In the previous chapter, all design parameters of the device except the transducer width, flow channel width and the distance of the flow channel from the transducer were determined based on various design considerations that did not involve calculation of any physical quantity in the acrylic cutouts and the flow channel. The remaining parameters mentioned above needed information from variables like pressure, velocity, displacement and electric fields for accurate calculation. Hence, FEA simulations were performed to obtain this information.

3.1) Quantifying the role of traveling waves and standing waves in the flow channel

Since the thesis aimed at designing a device that supports traveling waves in the flow channel, it was necessary to derive a coefficient that provides information about the relative role of traveling and standing waves at any point in the flow channel. A coefficientzeta 'ζ' was developed by Dr. Oleg Sapozhnikov for facilitating the same. Following is the derivation:

Consider a one-dimensional wave traveling along z-axis (refer figure 5 for z-axis). The instantaneous intensity of the wave is $\mathbf{I} = p\mathbf{v}$, where p is the acoustic pressure and $\mathbf{v}$ is the particle velocity. Due to the symmetry of the problem about the *z* axis, the intensity is directed along the *z* axis, that is, $I_z = pv_z$ is only non-zero.

Consider a sine wave. The acoustic pressure $p = p(x, y, z, t)$ can be expressed as follows:

$$p = \frac{P}{2} e^{-i\omega t} + \frac{P^*}{2} e^{i\omega t} \tag{4}$$

where $P = P(x, y, z)$ is the complex amplitude of the acoustic pressure, $\frac{\omega}{(2\pi)}$ is the frequency, and the asterisk denotes complex conjugate. The particle velocity can be expressed similarly. For instance, the *z*-component of the particle velocity has the following presentation:

$$v_z = \frac{V}{2} e^{-i\omega t} + \frac{V^*}{2} e^{i\omega t} \tag{5}$$

where $V = V(x, y, z)$ is the velocity complex amplitude. Note that the linearized momentum equation $\rho \frac{\partial v_z}{\partial t} = -\frac{\partial p}{\partial z}$ (where ρ is the medium density) can be used to express the velocity amplitude as

$$V = -\frac{i}{\rho\omega} \frac{\partial P}{\partial z} \tag{6}$$

In many cases of practical interest, an acoustic wave can be considered as being locally dependent mainly on one coordinate. Let it be the *z* coordinate. In this case, the complex amplitudes *P* and depend *V* only on *z*. For a sine wave,

$$P(z) = \frac{P_+}{2} e^{ikz} + \frac{P_-}{2} e^{-ikz} \tag{7}$$

If $|P_+| = |P_-|$ it is a standing wave, if $P_+ = 0$ it is a wave propagating to the left, and if $P_- = 0$ it is a wave propagating to the right. According to Eq. (6),

$$V(z) = \frac{\frac{dP}{dz}}{i\rho_0\omega} = \frac{1}{2\rho_0 c_0} \left(P_+ e^{ikz} - P_- e^{-ikz} \right) \tag{8}$$

Consider the acoustic intensity. The instantaneous intensity of the wave is $\boldsymbol{I} = p\boldsymbol{v}$, where p is the acoustic pressure and $\boldsymbol{v}$ is the particle velocity. Due to the symmetry of the problem, on the *z* axis the intensity is directed along the *z* axis, that is, $I_z = pv_z$ is only non-zero. Hence,

$$I_z = pv_z = \left(\frac{P}{2} e^{-i\omega t} + \frac{P^*}{2} e^{i\omega t} \right) \left(\frac{V}{2} e^{-i\omega t} + \frac{V^*}{2} e^{i\omega t} \right) =$$

$$\frac{PV}{4}e^{-2i\omega t} + \frac{P^*V^*}{4}e^{2i\omega t} + \frac{PV^*+P^*V}{4} = \frac{1}{2}Re\left(PV^* + PV\ e^{-2i\omega t}\right) \quad (9)$$

For example, if the wave is a traveling plane wave propagating along the *z* axis, then $V = \frac{P}{\rho_0 c_0}$ and $P = P_+ e^{ikz}$, where $k = \frac{\omega}{c_0}$ is the wavenumber. Hence,

$$I_z|_{\substack{\text{traveling}\\ \text{plane wave}}} = \frac{P_+^2}{2\rho_0 c_0}\{1 + cos[2(\omega t - kz)]\} = \frac{P_+^2}{\rho_0 c_0}cos^2(\omega t - kz) > 0. \quad (10)$$

If the wave is a standing plane wave, then $P = \frac{P_0}{2}\left(e^{ikz} + e^{-ikz}\right)$, $V = \frac{P_0}{2\rho c}\left(e^{ikz} - e^{-ikz}\right)$, and therefore

$$I_z|_{\substack{\text{standing}\\ \text{wave}}} = \frac{P_0^2}{4\rho c}sin(2kz)\,sin(2\omega t) \quad (11)$$

Here P_0 = P_+ = P_- is assumed to be real. During one half of the period of the wave $I_z|_{\substack{\text{standing}\\ \text{wave}}} > 0$, and during the other half $I_z|_{\substack{\text{standing}\\ \text{wave}}} < 0$. In average, $\langle I_z\rangle|_{\substack{\text{standing}\\ \text{wave}}} = 0$.

It was necessary to decide whether the wave is mostly traveling or mostly standing in a given point of space. A possible criterion could be based on the comparison of the oscillating (reactive) part of the acoustic intensity with the propagating (active) part of it. In particular, it would be convenient to introduce some coefficient that indicates whether the energy is mostly traveling to the left, to the right, or does not travel at all (a standing wave).

To introduce such a coefficient, consider $P = A_P e^{i\Phi_p}$ and $V = A_V e^{i\Phi_V}$, where $A_P = |P|$ and $A_V = |V|$ are positive quantities (real amplitudes), Φ_P and Φ_V are the corresponding phases. Then from Eq. (9) it follows that

$$I_z = \frac{1}{2}Re\left(PV^* + PV\ e^{-2i\omega t}\right) = \frac{A_P A_V}{2}Re\left(e^{i(\Phi_p - \Phi_V)} + e^{i(\Phi_p + \Phi_V)}\ e^{-2i\omega t}\right) =$$

$$\frac{A_P A_V}{2}\{cos(\Phi_P - \Phi_V) + cos[2\omega t - (\Phi_P + \Phi_V)]\} \quad (12)$$

Let us introduce

$$\varsigma = cos(\Phi_P - \Phi_V). \quad (13)$$

With the use of this coefficient, the instantaneous acoustic intensity takes the following form:

$$I_z = I_0\{\varsigma + cos[2\omega t - (\Phi_P + \Phi_V)]\} = \langle I_z \rangle + \tilde{I}_z \quad (14)$$

where $I_0 = \frac{A_P A_V}{2}$. It can be seen that while the reactive part of the intensity, $\tilde{I}_z = I_0\, cos[2\omega t - (\Phi_P + \Phi_V)]$, oscillates in time with amplitude I_0, the time-averaged (i.e., active) part of the intensity,$\langle I_z \rangle = \varsigma I_0$, does not. Therefore, the coefficient ς compares the standing and traveling components of the wave intensity and, as such, can be used to estimate the structure of a wave (standing or traveling) according to its local values of the complex amplitudes P and V. Note that when $\varsigma = -1$, the wave would be backward traveling wave, since the pressure and velocity are in opposite phases. When $\varsigma = 0$, the wave would be a standing wave, since the phase difference between pressure and velocity is 90^0. When $\varsigma = 1$, the wave would be a forward traveling wave since the phase difference between pressure and velocity is zero.

Following table provides the information about the interpretation of ζ:-

ζ value	**Type of wave**
-1	Backward traveling wave
0	Standing wave
1	Forward traveling wave

Table 1. Interpretation of values of ζ

Forward traveling wave travels in positive z-direction and backward traveling wave travels in negative z-direction (figure 2). In the next section, Finite Element Analysis simulations were performed and the coefficient ζ was used and a parameter for understanding the relative role of standing and traveling waves.

3.2) Two-dimensional simulations

Simulations using COMSOL Multiphysics 5.5 were performed to determine the optimal geometry for the device. In particular, results from previous manifestations of the device were difficult to interpret because the flow channel was in the acoustic near field of the transducer, making interpretation difficult. The current simulations were performed to find the optimum distance between the transducer and the flow channel such that it was in the far-field and the acoustic field would thus be monotonically decreasing with position. 2D simulations were performed in the YZ and ZX planes because the simulations could be performed quickly. A 3D simulation was later performed once the optimal parameters were obtained via the 2D simulations. The 3D simulation should be more accurate, but the cost of computational time and memory precluded us from using it exclusively.

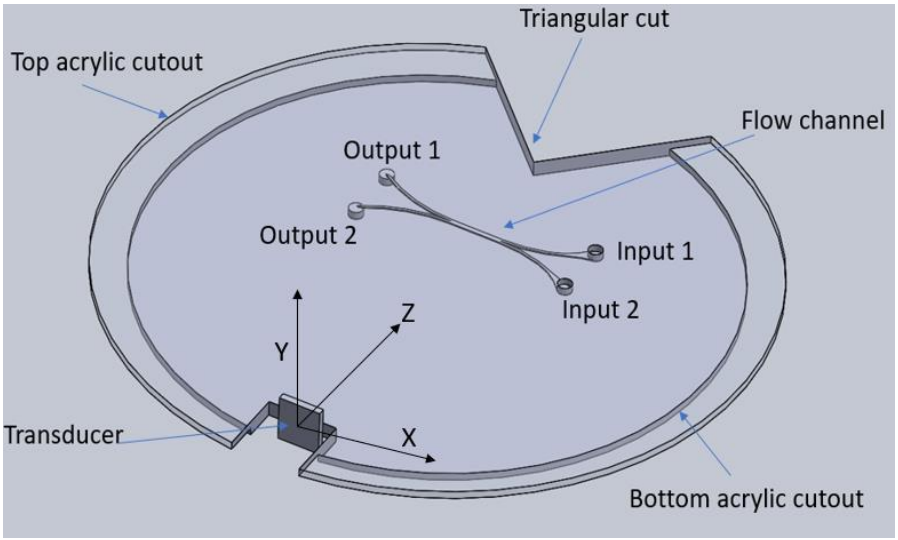

Figure 5. One of the possible designs of the cell sorting device

3.2.1) Geometry and materials

Simulation 1(YZ plane)

A section of the geometry in figure 5 was taken along YZ plane. Figure 6 shows the resulting geometry. The top acrylic cutout (CEHI) and the bottom acrylic cutout (EBGH) each were 70 mm along z axis and 1 mm along y axis. The transducer (ABCD) was mounted on the acrylic as described in chapter 4. The dimension AD was 2 mm while the dimension AB was 1 mm. The flow channel (KLMN) was placed at 20 mm distance from the transducer with KL=0.7mm and ML= 0.15 mm. The distance of the flow channel from the transducer will be optimized based on the simulations. An absorbing layer (JFGI) was placed at the location (66,0) to prevent reflections from the distal surface.

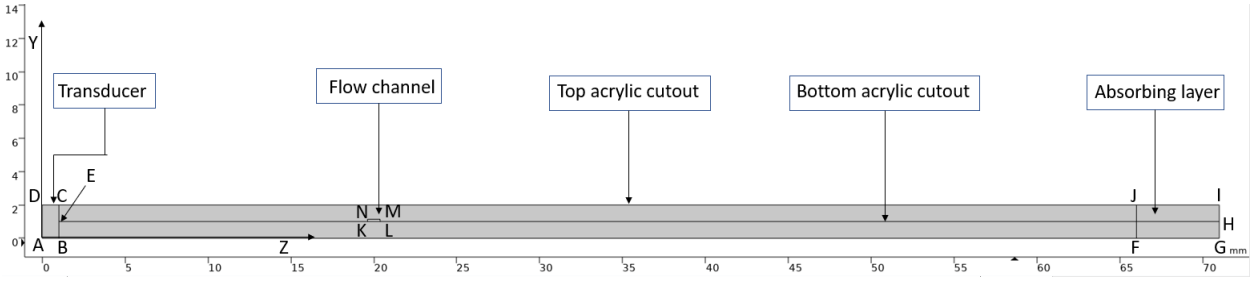

Figure 6. Simulation 1: 2D geometry

Simulation 2(XZ plane)

A section of the geometry in figure 5 was taken along ZX plane. Figure 7 shows the resulting geometry. The top acrylic cutout (STUWV) was visible from this view. The diameter of the top acrylic cutout was 90 mm. Point T was at 60 mm distance from the transducer and the angle STU was 90°. In this simulation, only the flow channel (OPQR) section in which the cell sorting process was going to occur was considered. The distance of the flow channel from the transducer was 45 mm which was varied in the simulation. The transducer (ABCD) was attached to the acrylic as

shown in the figure 7. Side AB was 10 mm, which will be varied in the simulations, whereas side BC was 1mm.

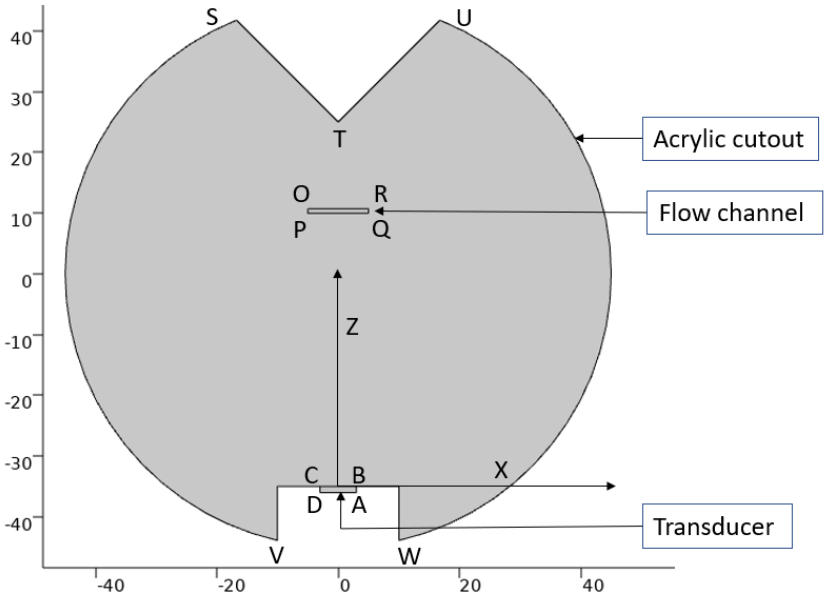

Figure 7. Simulation 2: 2D geometry

Materials

Table 2 lists the material selected for each component for both simulations. All materials were predefined in COMSOL.

Component	**Material**
Transducer	PZT-4
Cutouts	Acrylic
Flow channel	Water

Table 2. Two-dimensional simulations: Materials for each component

3.2.2) Physics and boundary conditions

Pressure acoustics, Frequency domain

The Pressure Acoustics, Frequency Domain interface is used to compute the pressure variations for the propagation of acoustic waves in fluids by solving the Helmholtz equation in the frequency domain [60]. This interface was applied to the flow channel domain since it is the location of interest. The pressure field in the flow channel domain was calculated and further used for the calculation of the ζ field. The flow channel domain was considered a linear elastic material, corresponding to a lossless compressible fluid.

Solid Mechanics

According to COMSOL, the Solid Mechanics (solid) interface in comsol is intended for general structural analysis of 3D, 2D, or axisymmetric bodies. In 2D, plane stress, plane strain, or generalized plane strain assumptions can be used. The Solid Mechanics interface solves the equations of motion together with a constitutive model for a solid material [61]. In our geometry, the solid mechanics interface was applied to the acrylic cutouts and the transducer. The displacement field was calculated which was further used to calculate the velocity and pressure fields. The acrylic cutouts were modeled as isotropic linear elastic material since acrylic is isotropic. Damping was introduced in the form of a loss tangent of 0.013 which was calculated from ref [66]. The transducer was modeled as apiezoelectric material poled in z-direction (refer figure 5 for z-direction).

Electrostatics

According to COMSOL, the electrostatics interface is used to compute the electric field, electric displacement field, and potential distributions in dielectrics under conditions where the electric

charge distribution is explicitly prescribed. The electrostatics interface solves Gauss Law for the electric field using the scalar electric potential as the dependent variable [62]. This interface was applied to the transducer since the electric field needed to be calculated to further calculate the displacement field.

Multiphysics

According to COMSOL, multiphysics is defined as systems involving more than one simultaneously occurring physical field [64]. In our simulations the electric field, as well as the displacement field, was solved for the transducer domain. In case of the flow channel, it shared a boundary with the acrylic cutouts. To simulate the effect of the pressure variations in the acrylic plates on the flow channel, their boundary was modeled as acoustic structure boundary, which couples the pressure acoustics interface and solid mechanics interface.

Modeling of the absorbing layer

According to COMSOL the perfectly matched layer (PML) is a domain or layer (sometimes called sponge layer) that is added to an acoustic model to mimic a nonreflecting domain. It sets up a perfectly absorbing domain as an alternative to nonreflecting boundary conditions. The PML works with all types of waves, not only plane waves. It is also efficient at very oblique angles of incidence[65]. In simulation 1, domain (JFGI) was modeled as a perfectly matched layer. This corresponds to the triangular cut made in the acrylic cutouts built to prevent any reflections towards the flow channel.

Table 4 shows the physics applied to each component for two-dimensional simulations.

Component	**Physics**
Transducer	Solid Mechanics (piezoelectric material) Electrostatics
Acrylic cutouts	Solid Mechanics (linear elastic material)
Flow channel	Pressure acoustics, Frequency Domain

Table 3. Two-dimensional simulations: Physics applied to each component

Pressure release boundary condition

Figures 8 and 11 show pressure release boundary conditions for acrylic cutouts and the transducer for simulations 1 and 2. The pressure release boundary (pressure=0) is applied to the areas of the transducer and acrylic cutouts exposed to air, since the pressure at the boundary is zero due to complete reflection of sound wave into the acrylic cutouts and transducer. The complete reflection is due to impedance mismatch between the acrylic and air. Acoustic impedance is a product of the density and speed of sound of the material. The reflections between two materials are fewer if their impedance matches and vice versa.

Absorbing boundary conditions

Figure 9 and 10 display low reflecting boundary conditions and absorbing boundary for simulation 1. As mentioned before, domain JFGI (figure 6) was modeled as an absorbing layer. Side IG was considered as a low-reflecting layer to further enhance the absorbing capacity of the modeled PML. Low-reflecting boundary conditions takes the material data from the adjacent domain in an attempt to create a perfect impedance match for both pressure waves and shear waves.

Electric potential

1V potential was applied to the side of the transducer exposed to air, and the side of the transducer attached to acrylic was grounded for both simulations.

Figure 8. Simulation 1: Pressure release boundary condition highlighted in blue

Figure 9. Simulation 1: Perfectly matched layer (absorbing boundary) highlighted in blue

Figure 10. Simulation 1: Low-reflecting boundary highlighted in blue

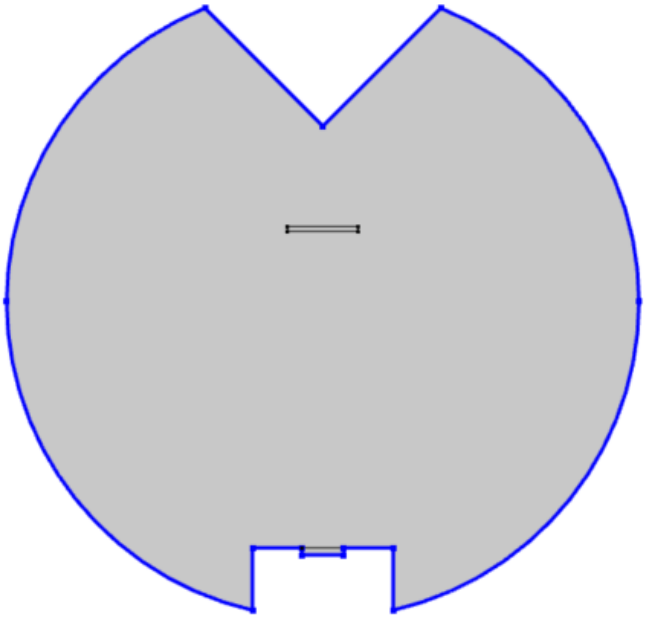

Figure 11. Simulation 2: Pressure release boundary condition highlighted in blue

3.2.3) Mesh and solver specifications

Quadrilateral mesh consisted of square elements whereas free triangular mesh consisted of variable sized triangular elements. A quadrilateral mesh was applied for the transducer domain (ABCD). A free triangular mesh was applied to the domain corresponding to acrylic cutouts (CBGI), since this type of mesh enables low element size, increasing accuracy. To keep the continuity of mesh type, the acrylic cutouts were modeled as free triangularelements. Figure 12 shows the meshing of the domain near the flow channel.

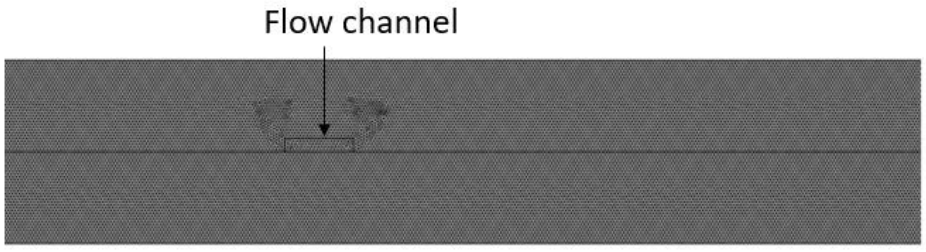

Figure 12. Mesh near the flow channel

Determination of mesh size

The determination of optimum mesh size was important because we needed an accurate solution in a reasonable computational time. In this study, the mesh size was determined with respect to the wavelength of sound wave. Since the wavelength of a sound wave in water was lower as compared to the wavelength of sound in plastic and PZT-4 at a specific frequency, the mesh refinement study was performed with respect to the wavelength of sound in water for maximum accuracy.

Element size determination for simulation 1 (along YZ plane)

A mesh refinement study was performed to obtain the element size at which the relative percent error in the solution would be less than 0.1 percent, which was considered the acceptable error in our simulations. The solution parameters were 'ζ' in the flow channel and the average pressure in the plates. A mesh refinement parameter 't' was introduced for this study, the value of which was increased from ten to thirty in increments of one. Solutions were obtained for each element size and percent error was calculated relative to element size wavelength/30. The result plots are shown in figure 13 and figure 14. In both plots, the solution parameter crosses 0.1 percent after t=20. Hence, the value of mesh refinement parameter was finalized at 20 and the consequently, the mesh size was finalized at 20 elements per wavelength.

$$Element\ size = \lambda/t \tag{15}$$

Where t= mesh refinement parameter

λ =wavelength of sound in water

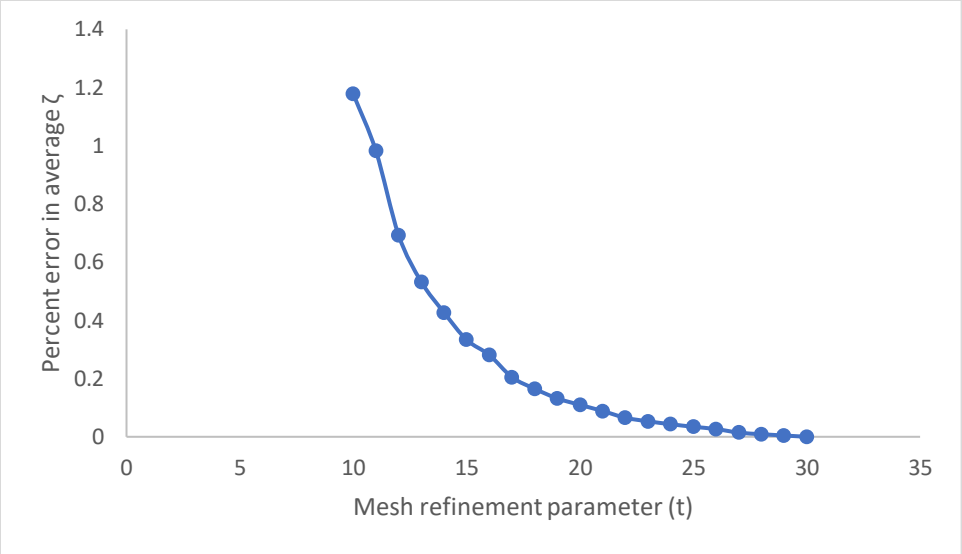

Figure 13. Mesh refinement study. Solution parameter: ζ

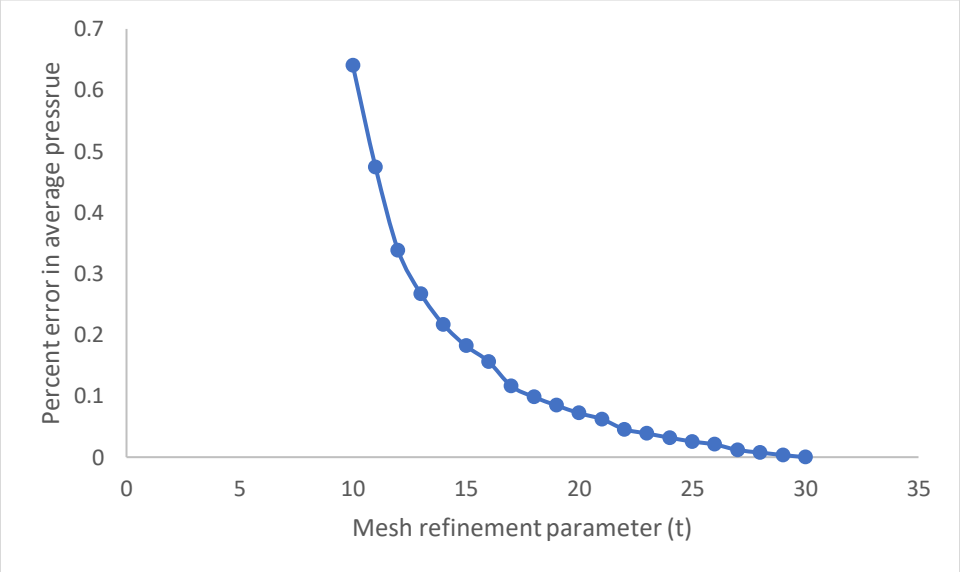

Figure 14. Mesh refinement study. Solution parameter: average pressure

Element size determination for simulation 2 (XZ plane)

The mesh size for this simulation was fifteen elements per wavelength, which was the minimum mesh size possible with memory and computational time constraints

Solver specifications

A frequency domain study was conducted with 2 MHz frequency, which was determined in chapter 2. The simulation was solved using a fully coupled solver approach with the solver 'PARDISO'.

Solver specifications for simulation 1

A parametric sweep was conducted by changing the parameters flow channel width, flow channel height, and distance of the flow channel from the transducer. Although the height and width of the flow channel were already finalized in the design section, it was necessary to include them in the simulation for obtaining more information about their trends. Table 5 shows the range of the three parameters which resulted in a total of 210 combinations. (Appendix A2)

Parameter	Start (mm)	Increment (mm)	Stop (mm)
Length	0.5	0.1	1
Height	0.1	0.05	0.3
Distance from transducer	20	5	50

Table 4. Simulation 1: Parametric sweep

Solver specifications for simulation 2

Variation of average ζ in the flow channel was determined with the distance of flow channel from the transducer since it was needed to be evaluated whether simulation 2 gives similar trends as simulation 1. In addition to this, the transducer (AB) width was varied to determine the effect on ζ in the flow channel. Furthermore, inlets and outlets were modeled to evaluate their effect on the acoustic field in the flow channel.

Parameter	Start(mm)	Increment(mm)	Stop(mm)
Distance of flow channel from transducer	5	10	45
Width of the transducer	4	1	10

Table 5. Simulation 2: Parametric sweep

3.3) Two-dimensional simulations-Results

Pressure field in acrylic cutouts (simulation 1, along YZ plane)

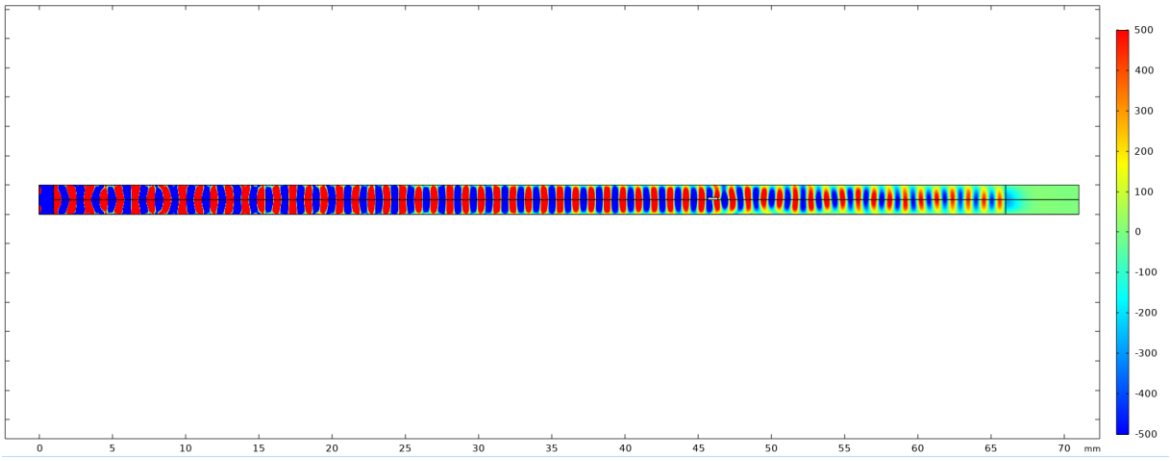

Figure 15. Simulation 1: Pressure field in the acrylic cutouts (Pa)

We plotted the pressure field in the acrylic cutouts to visualize the distance at which near field transitions to far-field. Figure 15 shows the pressure field in the plates in Pascals which was calculated as the negative trace of the diagonal elements of the stress tensor. We could see the transition of the near field to far field which is monotonically changing with the position after 30 mm from the transducer. This implied that placing the flow channel after 30 mm would be advisable, but more data was needed to confirm this decision.

Variation of Average ζ with distance (simulation 1, along YZ plane)

As stated in chapter 1, this research aims to fabricate a device capable of supporting traveling waves in the flow channel. 'ζ', a parameter for calculating traveling and standing wave components at each point in the flow channel is developed at the beginning of this chapter. To calculate the role of standing wave and traveling wave components in the whole flow channel, we averaged the ζ value of all points in the flow channel for each distance. From Table 1, we note that as the value of ζ approaches 1, the conditions tend towards a forward travelling wave.

Figure 16 shows the variation of average ζ in the flow channel with the distance from the transducer. Fluctuations in average ζ were observed in the near field which considerably reduced after 30 mm distance, indicating that there is a high probability that forward traveling wavesdominate in the flow channel after 30 mm distance. Minimum ζ in the flow channel was also plotted in figure 17 to investigate the possibility of backward traveling waves at any points inside the flow channel in far field, since average ζ alone does not provide complete information about the relative role of traveling and standing waves. It was observed that the minimum ζ is positive after 25 mm distance suggesting that backward traveling waves are not present in the far field. As a summary, figures 16 and 17 indicate a high probability of forming forward traveling waves in the flow channel after 30 mm distance from the transducer.

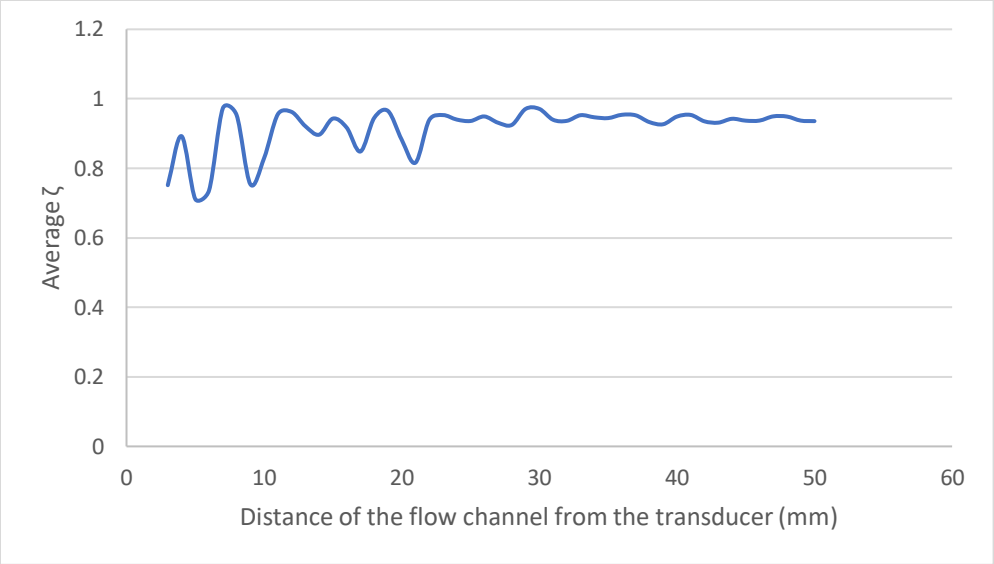

Figure 16. Simulation 1: Average ζ in flow channel vs Distance of flow channel from transducer

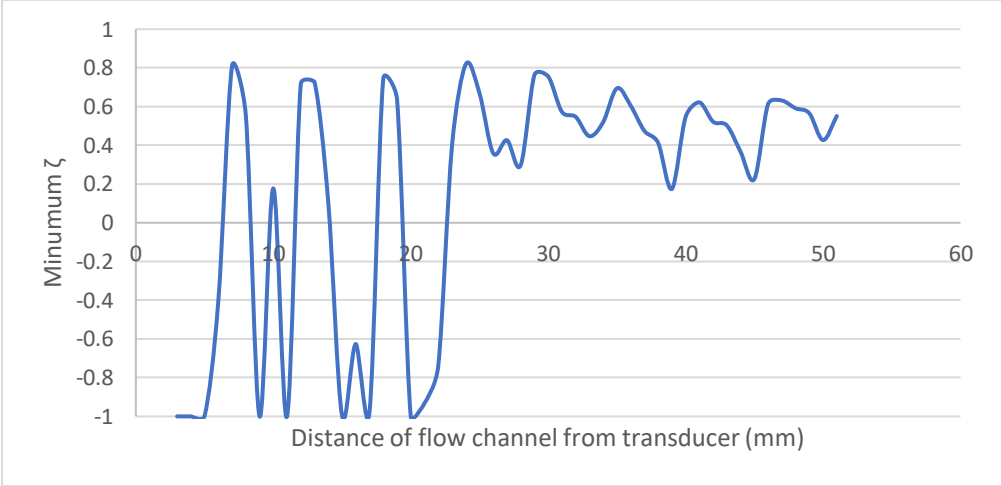

Figure 17. Simulation 1: Minimum ζ in the flow channel vs Distance of flow channel from transducer

The results from simulation 1 provided valuable insights for the placement of the flow channel. One of the reasons for performing the second simulation was evaluating whether the trends are similar to that of simulation 1.

Pressure field in the acrylic cutouts (simulation 2, along XZ plane)

It was necessary to plot the pressure field in the acrylic cutouts to get an idea of the distance at which near field transitions to far-field. Figure 18 shows the pressure field in the plates which was calculated as the negative trace of the diagonal elements of the stress tensor. We could see the transition of the near field to far field which is monotonically changing with the position after 20 mm from the transducer.

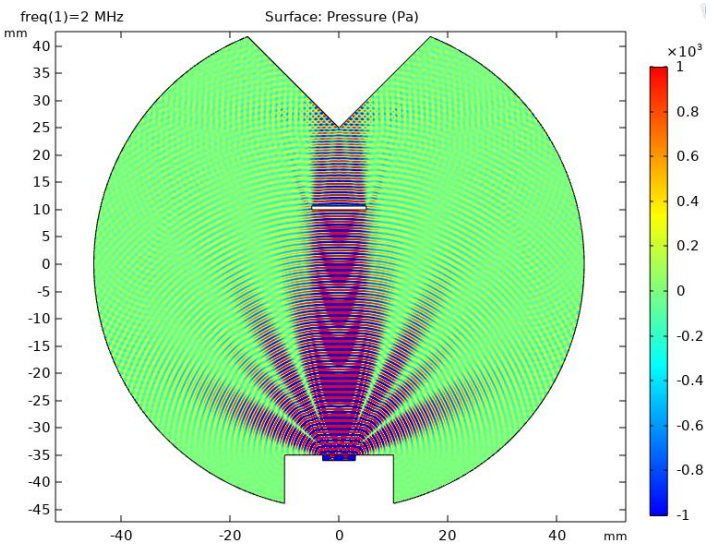

Figure 18. Simulation 2: Pressure field

Variation of Average ζ with distance (simulation 2, XZ plane)

It was necessary to compare the trends of average ζ of simulation 2 with that of simulation 1. Figure 19 shows the variation of average ζ in the flow channel with its distance from the transducer for simulation 2. The average ζ stabilized at 20 mm after some fluctuations in the near field. This plot was similar to that of simulation 1 (figure 20), further solidifying the decision of placing the flow channel in the far-field. Minimum ζ in the flow channel was plotted for simulation 2 for the same reasons mentioned in simulation 1. We could see that the value of minimum ζ in the flow

channel is greater than zero after 40 mm distance, suggesting the existence of forward traveling waves and standing waves but no backward traveling waves.

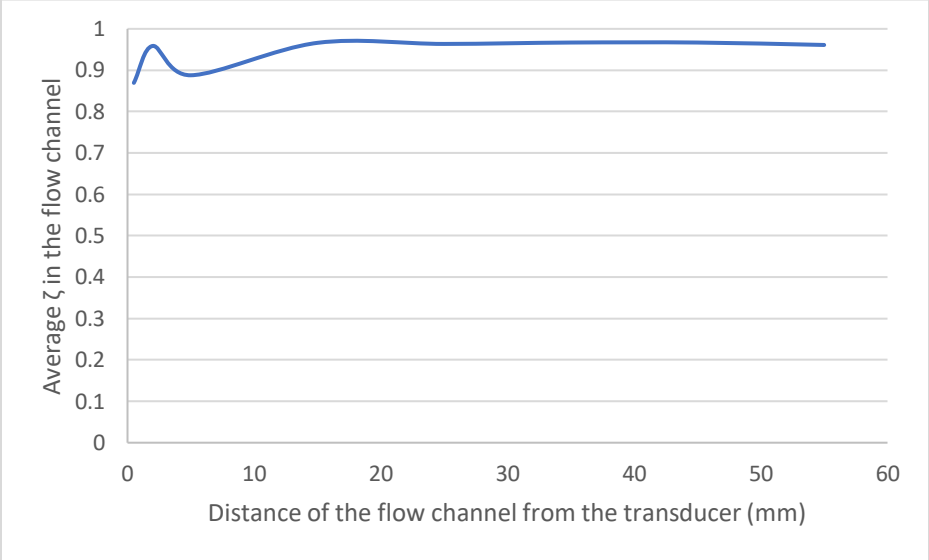

Figure 19. Simulation 2: Average ζ in flow channel vs Distance of flow channel from transducer

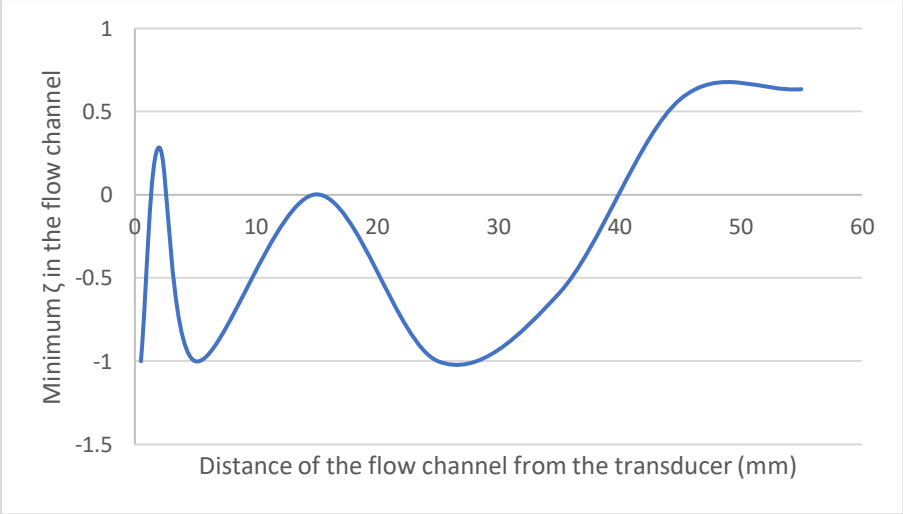

Figure 20. Simulation 2: Minimum ζ in the flow channel vs Distance of flow channel from transducer

At this point, the distance of the flow channel was finalized at 45 mm. Although 2D simulation results indicate that any distance after 30 mm is acceptable, the flow channel was placed at 45 mm

because the average ζ plot stabilizes further after 40 mm in simulation 1(figure 16). In addition to this, the value of minimum ζ in simulation 2 is positive only after 40 mm distance.

3.3.5) Change of length of transducer vs average ζ (simulation 2 XZ plane)

Although the height (side AD simulation 1, figure 6) of the transducer was finalized in chapter 2, the transducer width (side AD simulation 2, figure 7) was needed to be finalized. To enable this, average value of ζ in the flow channel was evaluated for transducer widths ranging from 4 mm to 10 mm (Figure 21). We could observe that value of average ζ is independent of the width of the transducer between 4mm to 10mm. Hence, selection of any width was acceptable. The width of the transducer was finalized as 6 mm. Since the distance of the flow channel was already optimized, the flow channel was placed at 45 mm for this study.

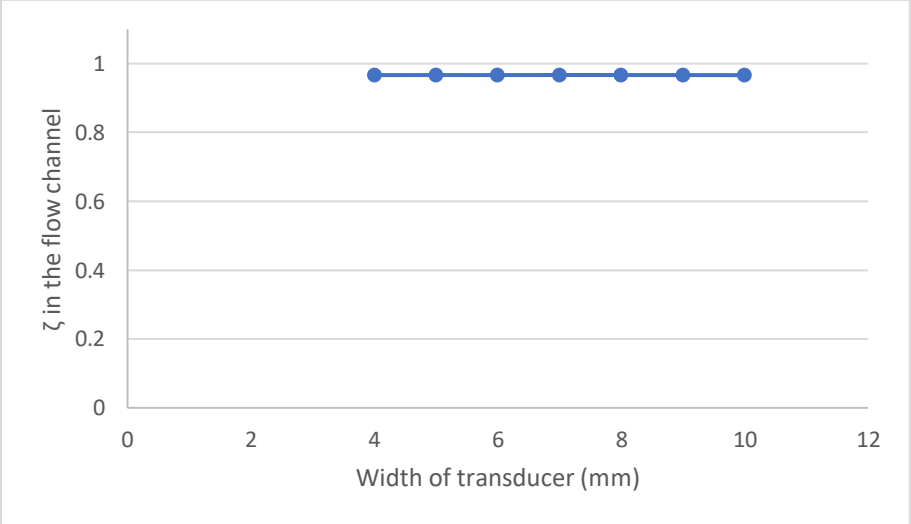

Figure 21. Simulation 2: Average ζ in the flow channel vs Width of transducer

Incorporation of inlet and outlet masses

Although the inlet and outlet ports labeled in figure 5 were not included in the 2D simulations, it was important to study their effect on the ζ field and the average ζ in the flow channel, because the additional masses of plastic tubes attached to the ports could disturb the acoustic field leading to unwanted reflections. Detailed fabrication process of attaching plastic tubes to inlet and outlet ports is provided in chapter 4. Also, they could not be modeled in simulation 1 since they are not visible from that section view.

Four circles representing the inlet and outlet tubes were introduced as shown in figure 22. The circular domains were selected with predefined water as their material representing the water in the tubes. The width of transducer was 6 mm and the flow channel was placed at 45 mm. All the remaining specifications were same as that of simulation 2.

Table 5 shows the comparison of average ζ with and without the incorporation of inlets. Since the average ζ is equal for both, we concluded that the inlets and outlets do not create any changes in the role of standing and traveling waves in the flow channel.

	Average ζ in the flow channel
Without inlets and outlets	0.9669
With inlets and outlets	0.9657

Table 6. Comparison of Average ζ in flow channel

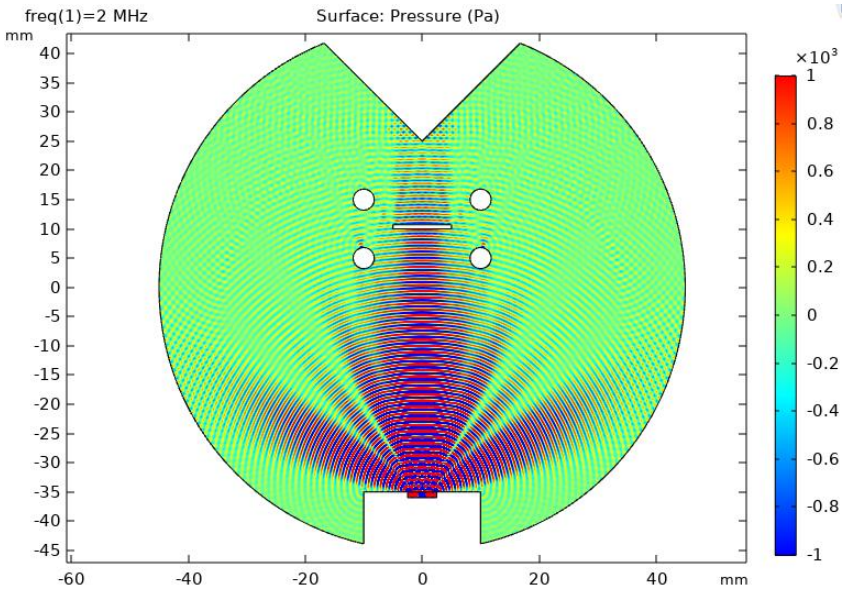

Figure 22. Pressure field in the cutout (inlets and outlets included)

3.4) Three-dimensional simulations

Although simulating on two-dimensional geometries provided valuable insights for optimizing the width of the flow channel and its distance from the transducer, it was necessary to validate them by simulating on a three-dimensional geometry. A truncated three-dimensional geometry was used for validating the final dimensions of the flow channel obtained from the two-dimensional geometries. Following are the steps for simulating three-dimensional geometry.

3.4.1) Geometry and materials

In general, a large amount of memory is needed for three-dimensional simulations. Methods like exploiting symmetry, truncation of the domain, and avoiding complicated geometries are used for reducing the required memory without compromising accuracy. As shown in figure 23, we truncated the domain and applied the necessary boundary conditions that will be discussed in the physics section. In addition, we exploited the symmetry by modeling one-fourth of the truncated geometry since preliminary simulations showed that the acoustic field is symmetric about the XZ

plane and the YZ plane. The dimensions of acrylic cutouts are the same as mentioned in two-dimensional simulations.

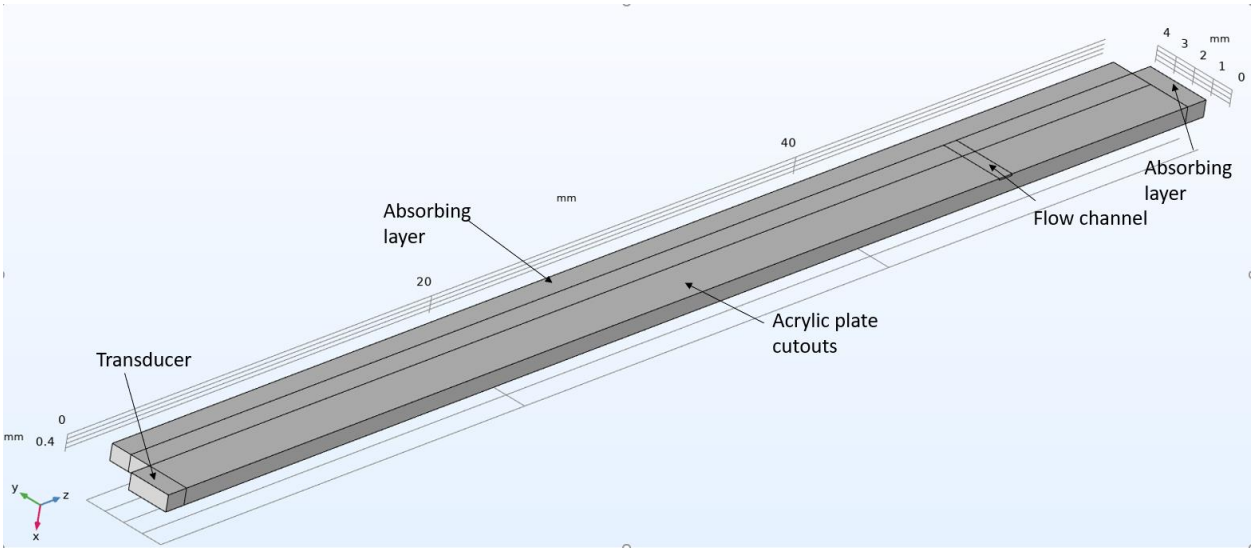

Figure 23. Three-dimensional simulation: Geometry

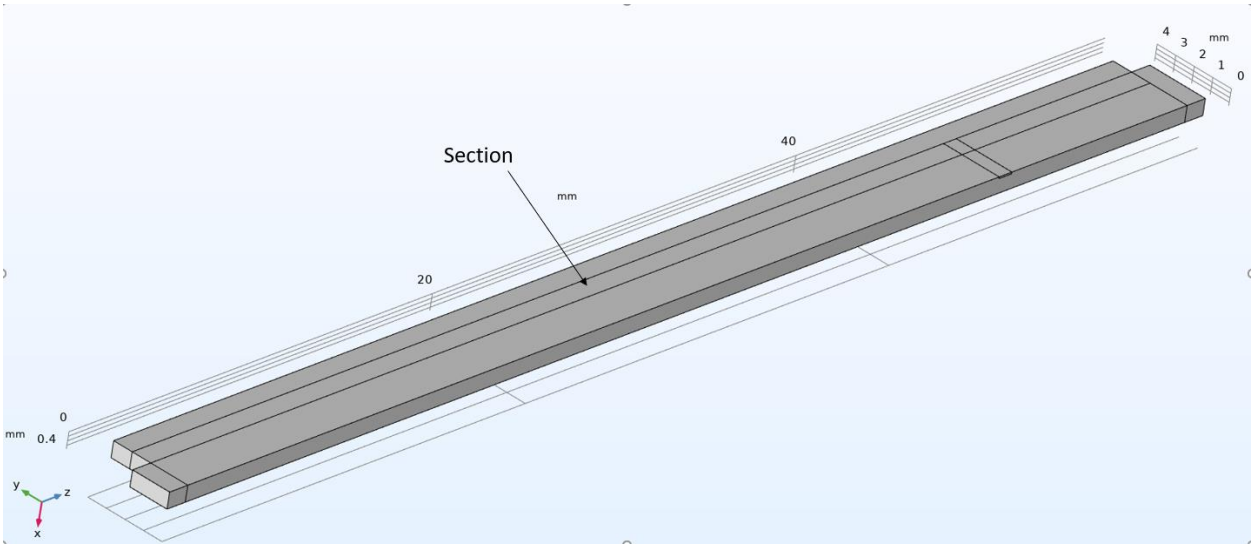

Figure 24. Three-dimensional simulation: Section added for easy meshing

Figure 24 shows a sub-domain labeled as ‘section’ in acrylic. The sub-domain is created to facilitate the use of a swept mesh. An important rule for employing a swept mesh is that the area

of sweep should remain constant, which was only possible by creating a sub-domain. For solver purposes, the sub-domain was a part of acrylic plate cutout.

Materials

Component	Material
Transducer	PZT-4
Cutouts	Acrylic
Flow channel	Water

Table 7. Three-dimensional simulation: Materials for each component

3.4.2) Physics and boundary conditions

Table 7 shows the physics applied to the components. All components had the same interfaces as 2D.

Component	Physics
Transducer	Solid Mechanics (piezoelectric material) Electrostatics
Acrylic cutouts	Solid Mechanics (linear elastic material)
Flow channel	Pressure acoustics, Frequency Domain

Table 8. Three-dimensional simulation: Physics applied to each component

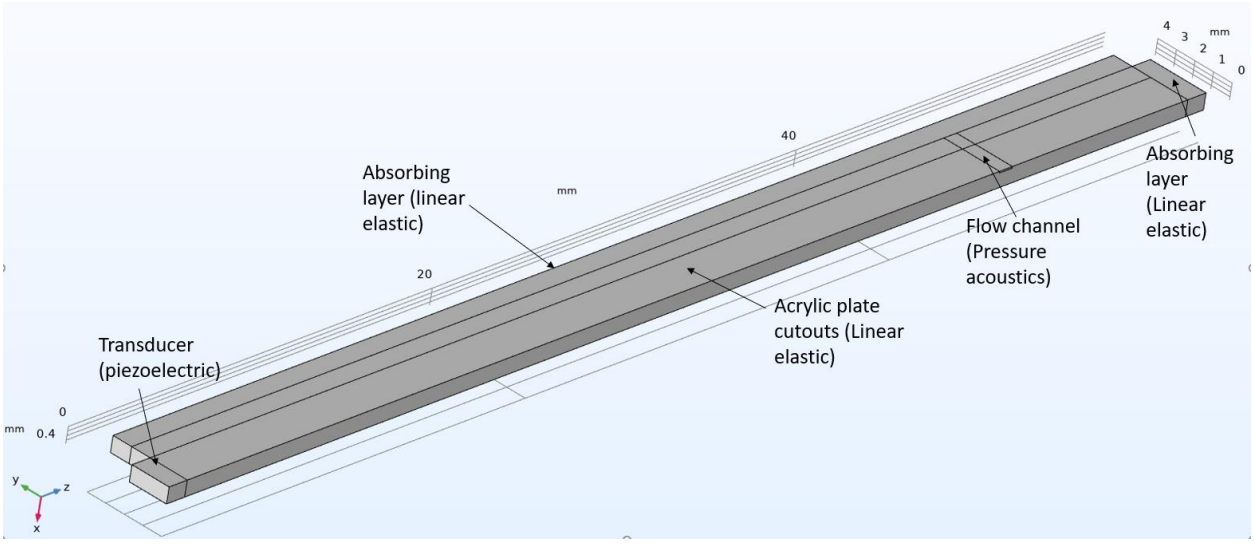

Figure 25. Three-dimensional simulation: Physics for each domain

Boundary conditions

We assumed that there would be no reflections from the boundary of the plates. Hence, we truncated the geometry and applied an absorbing boundary condition by modeling the truncated sub-domains as perfectly matched layers. The outside faces of these sub-domains were modeled as low reflecting boundaries to ensure that the faces will not reflect waves inside.

Symmetry

Figures 26 and 27 display symmetry boundary condition used for the flow channel as well as the acrylic plate cutouts. The highlighted region shows the faces about which symmetry was applied.

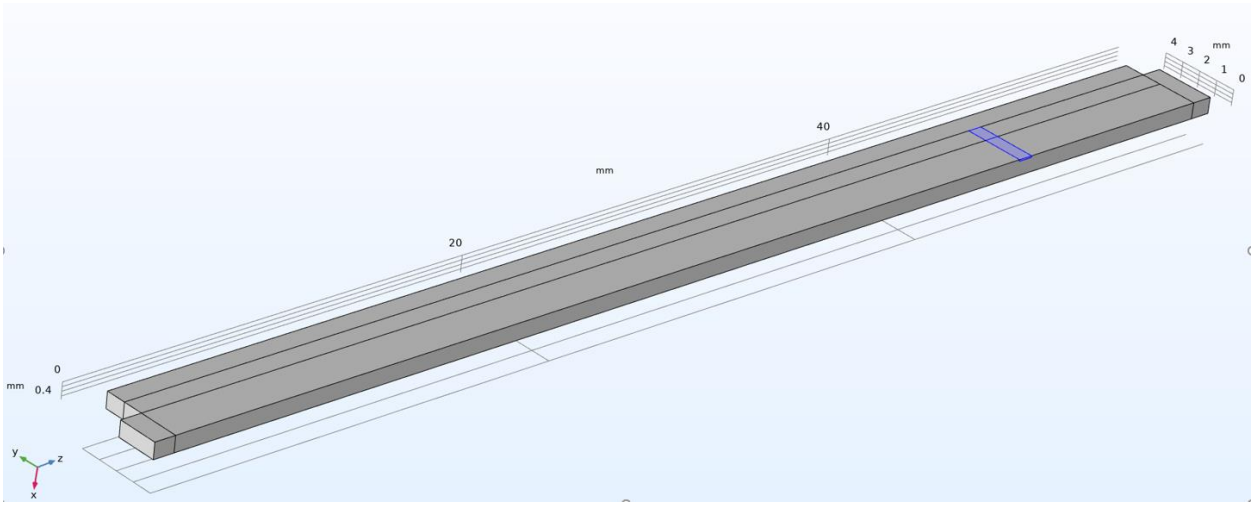

Figure 26. Three-dimensional simulation: Symmetry boundary condition for flow channel highlighted in blue

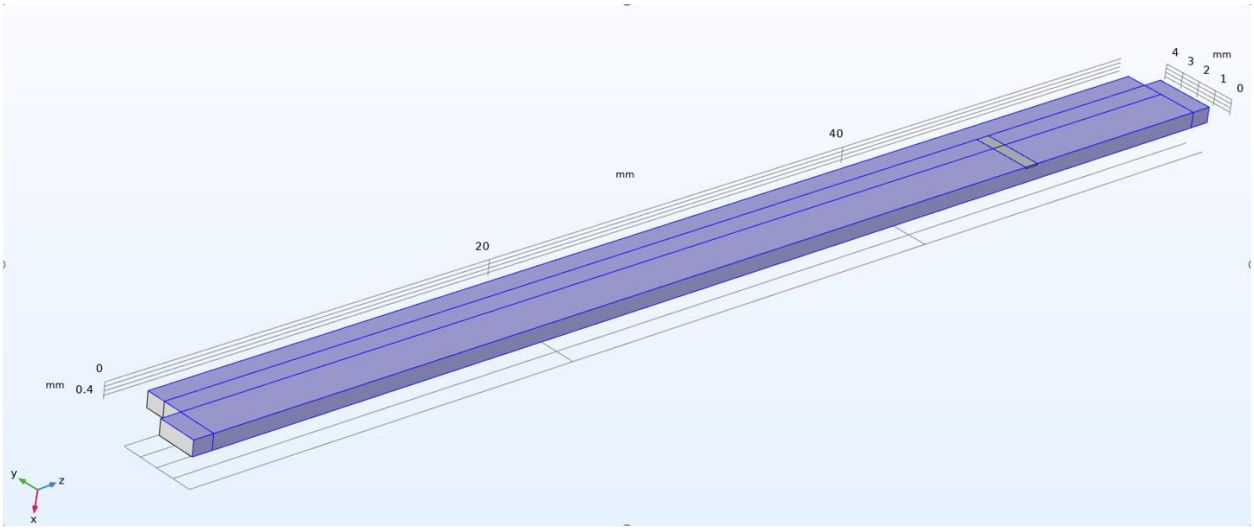

Figure 27. Three-dimensional simulation: Symmetry boundary condition for acrylic cutouts highlighted in blue

3.4.3) Mesh and solver specifications

A swept mesh was employed. We could not perform a mesh refinement study for three-dimensional geometry because of memory and time limitations. Hence, the lowest possible mesh size within the memory limitations was considered. The mesh size was wavelength of longitudinal wave in acrylic divided by ten. A frequency domain study was conducted with 2 MHz frequency, which was determined in chapter 2. The simulation was solved using a fully coupled solver approach with the solver ‘PARDISO’.

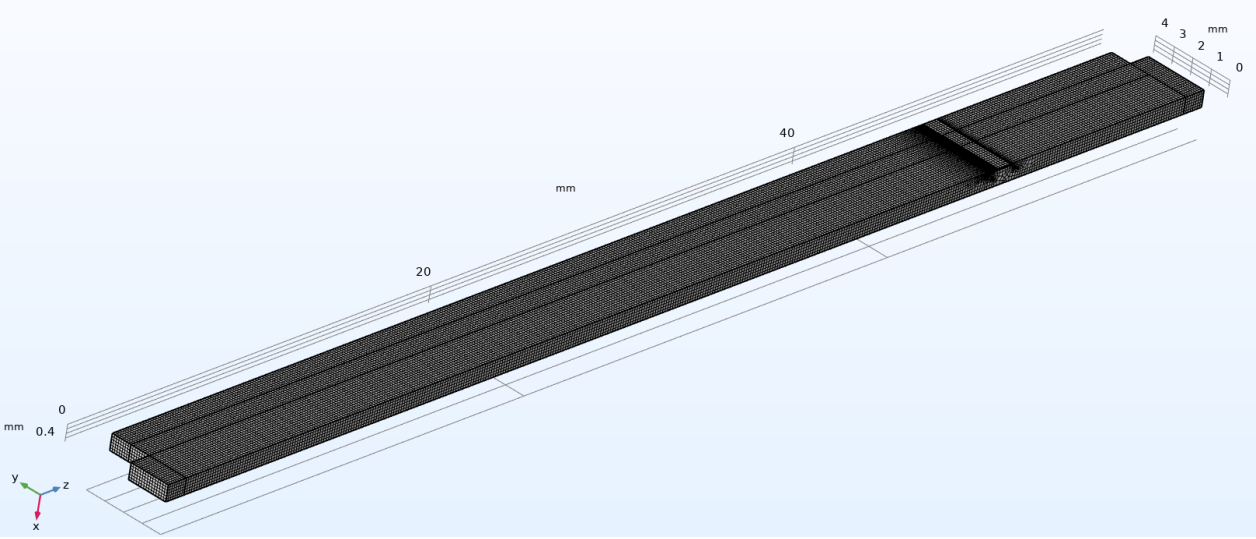

Figure 28. Three-dimensional simulation: Mesh

3.5) Three-dimensional simulations- Results

Since the aim of simulating three-dimensional geometry was to validate the two-dimensional geometries, we only calculated the ζ field in the flow channel for the optimum combination, and pressure field in the plates.

ζ field

Figure 29 shows the ζ field in the flow channel. We can see that it mostly shows forward traveling waves which is desirable. The average ζ is 0.85.

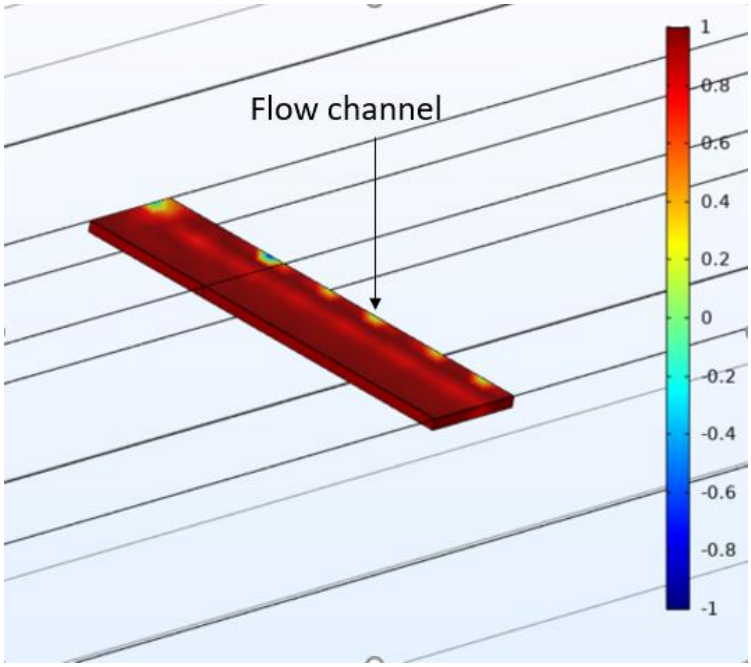

Figure 29. ζ field in the flow channel (close up view)

Pressure field in the acrylic plate cutouts

Figure 30 shows the pressure field in the acrylic plate cutouts. We can clearly see the near field transitioning into a uniform wave field.

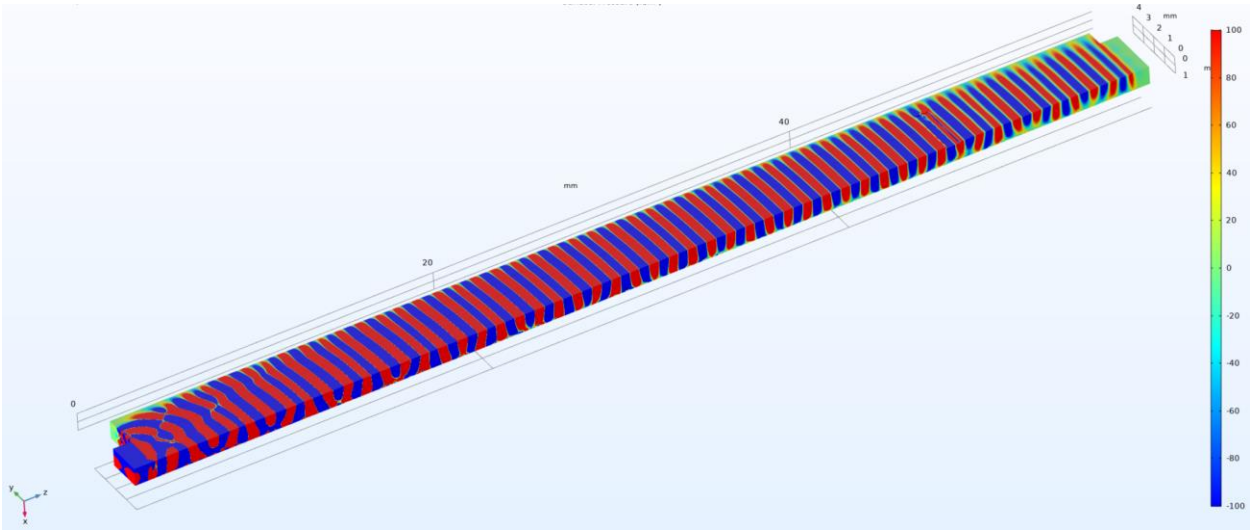

Figure 30. Three-dimensional simulation: Pressure field in acrylic cutouts (Pa)

3.6) Summary

To summarize, we optimized dimensions of the device to increase the probability of obtaining forward traveling waves in the flow channel. A coefficient was developed for providing information about relative role of standing waves and traveling waves in the flow channel. Two-dimensional simulations were performed by considering geometries sectioned by two perpendicular planes along the device. Results indicated that placing the flow channel in far-field, i.e after 40 mm distance from the transducer would increase the probability of obtaining traveling waves in the flow channel. Studies for optimizing the transducer width and evaluating the effect of inlet and outlet masses on pressure field were also performed. Results suggested that changing transducer width does not affect the pressure field in the flow channel. Also, the inlets and outlet masses do not affect the pressure field in the flow channel. The distance of the flow channel from the transducer was finalized at 45 mm, whereas transducer width was finalized at 6 mm. Three dimensional simulations were performed in order to validate the finalized dimensions in two dimensional simulations. Since the three-dimensional simulations also showed forward traveling waves for the specific combination, we concluded that two dimensional and three-dimensional simulations do not contradict each other. At this point, the dimensions of the device were finalized.

3.7) Limitations of the simulations

After finalizing most of the dimensions of the device in the design section, remaining dimensions were optimized by performing FEA simulations. The simulations only served as a guide since the dimensions were determined based only on trends in ζ. The simulations were not an accurate representation of reality because of the following discrepancies between simulations and reality.

1) Possibility of formation of microcracks in the acrylic cutouts during laser cutting which would lead to unexpected changes in the pressure field.

2) Epoxy was used for coupling the transducer to the acrylic cutouts, but was not modeled in the simulations.

3) The height of PZT was modeled to be equal to the total height of the acrylic cutouts (2 mm) in the simulations but was 6 mm in reality to enable solderingelectrical connections.

4) Mass of the soldering filler material attached to the transducer in the experiments were not accounted for in the simulations.

5) 2D model assumed that acoustic variables are constant in the direction perpendicular to the 2D plane, which was not true.

6) 3D model incorporated more features than the 2D model, but it was truncated and thus information about solution accuracy could not be obtained.

Chapter 4. Fabrication of the device

In order to test the results predicted by the simulations, it was necessary to fabricate the device. The basic fabrication process flow was imitated from the previous iterations of the device. Unfortunately, documentation of the process parameters was not available. Hence, the process parameters had to be optimized once more. The manufacturing processes used for fabricating the device were laser cutting, micro-machining and thermal bonding. Following is a detailed description of the fabrication process.

4.1) Laser cutting

Laser cutting is a manufacturing process that consists of slitting a metallic or non-metallic raw material by a laser beam of a high power-density. When the laser beam is concentrated on one point, more heat is introduced in the area than can dissipate through heat conduction. This causes the penetration of laser beam in the workpiece. Advantages of laser cutting over other cutting processes include high accuracy, wide material range and contour freedom [68]. Due to these advantages, laser cutting was employed for cutting the acrylics.

Figure 31 shows the cutouts laser cut from an acrylic sheet. BOSSLASER 1630 machine was used for cutting the acrylic. The cutting speed of the laser head was 15 mm/s since it was observed that this speed facilitates accurate cutting of acrylic sheets. 203*254 mm size acrylic sheets of 1mm thickness were cut into three pairs of small and large cutouts. A specific pattern of cutting was applied to fit maximum cutouts in one acrylic sheet. Although one pair of cutouts was sufficient to fabricate the device, numerous pairs were needed to account for the iterative acrylic bonding process.

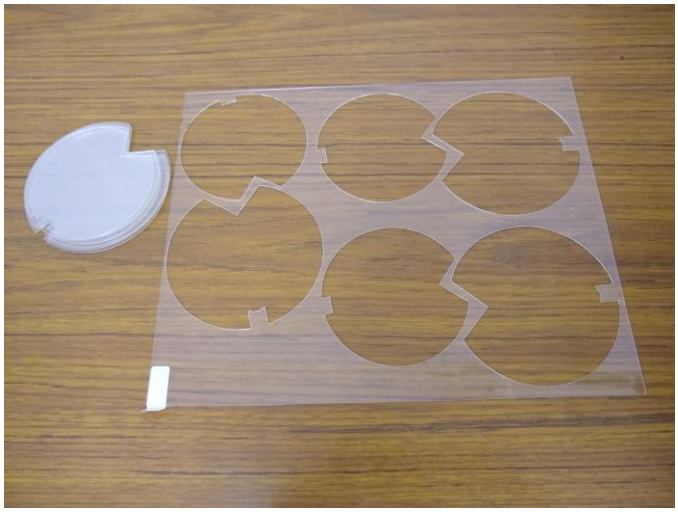

Figure 31. Cutouts laser cut from an acrylic sheet

4.2) Machining

A flow channel was required to be created in the acrylic cutouts. Possible manufacturing processes included soft lithography, photolithography, and micro-machining. Micro-machining was selected for creating the flow channel since the required infrastructure was available in our laboratory. As shown in figure 32, a flow channel was machined on the upper acrylic cutout. Subsequently, holes were drilled in both acrylics as shown in figure 32. The holes and the flow channel were machined

such that bonding of the two machined acrylic cutouts would result in an enclosed flow channel with inlet and outlet ports as shown in figure 38.

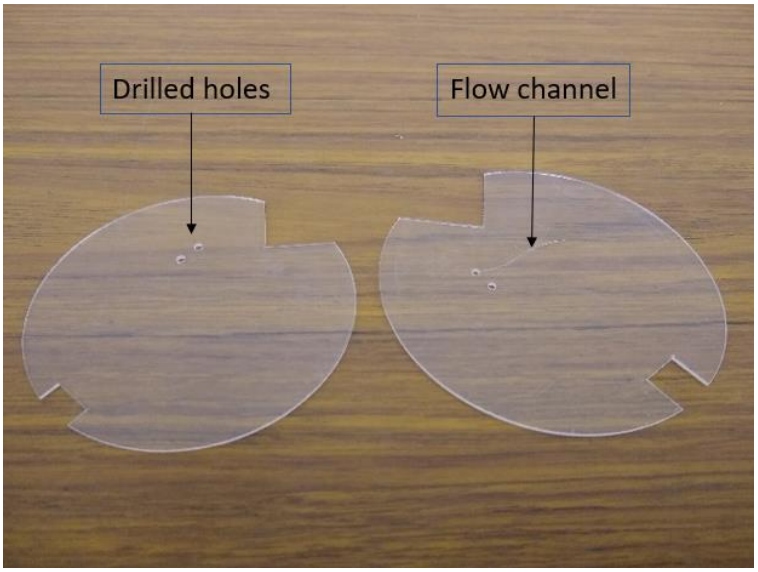

Figure 32. Machined acrylics; left: Lower acrylic cutout; Right: Upper acrylic cutout

4.2.1) Measuring the height of flow channel

Although the machining process was accurate, it was necessary to measure the height of the flow channel after machining to account for changed dimensions in case of end-mill bit breakage during the process. For measuring the height of the flow channel, a microscope with 10x objective lens was used. The microscope was focused on the bottom of the flow channel, and then on the top surface of the acrylic plate on which the flow channel was machined, and the number of turns of the focus knob were noted. The microscope was then calibrated by carrying out the same process for a transparent device of a known height. All dimensions of flow channel met expectations.

4.2.2) Machining specifications

An image of the flow channel machining process is shown in figure 33. Machining was performed on ACCUPATH ACCU 2 CNC milling machine. Ultratool 2 flute square micro end mill bit was used. Table 1 displays the machining parameters. More details about micro-machining are provided in appendix A1.

Parameter	**Value**
RPM	2000
Feed rate	0.5 inch/min
End-mill bit	2 flute
End-mill bit diameter	0.013 inch

Table 9. Machining specifications

Figure 33. Machining of the flow channel

4.3) Acrylic bonding

As mentioned in the section 4.2, acrylic bonding was required for enclosing the flow channel. Some of the methods for acrylic bonding include thermal fusion bonding, using chloroform along with thermal fusion bonding, or applying an acrylic softening glue. Thermal fusion bonding method was used for bonding the machined acrylic cutouts [67]. Methods consisting of chloroform

and glue were not used since there was a chance of flow channel deformation due to over-softening.

In our study, heat, pressure and time needed to be optimized to achieve an acrylic bond without air bubbles, and without deformation of the flow channel. This study was performed in a Quincy lab model 20 oven. An iterative study was performed until an optimized combination of pressure, temperature and time was obtained with repeatable results. An apparatus (figure 34) was used to apply pressure on the acrylic cutouts. Here, the pressure was applied with clamps. Hence, instead of measuring the pressure, the study was conducted in terms of torque on the clamps, because the pressure on the acrylic cutouts increases with increase in the torque on the clamps.

The assembly was placed inside an oven for a specific amount of time at a particular temperature. Following are the steps for assembling the apparatus.

Figure 34. Part A- Silicon rubber for Positioning. Part B & C- Silicone rubbers for force distribution. Part D & E- Aluminum clamps. Part F & G- Glass plate. Part H and I- acrylic cutouts Part M & L- Steel plates. Part J & K- Aluminum bars. Part N-Nuts and bolts

1) The apparatus was cleaned with iso-propyl alcohol to remove contaminants on the surfaces which may cause difficulties in acrylic bonding process.
2) A steel plate was placed on a flat table.
3) Silicone rubber was placed in the center of the steel plate. The rubber was used to apply a uniform pressure distribution on the acrylic cutouts.
4) The glass plate was placed over the silicone plate to insulate the acrylic cutouts, since the temperature of the glass plate was high after keeping it in the oven.
5) A matching silicone marker was placed on the glass plate for correct positioning of the acrylic cutouts with respect to the glass plates.
6) Large acrylic cutout was then placed onto the silicone marker. As mentioned in chapter 2, it was necessary to have a ledge over the mounting apparatus, hence one cutout was intentionally cut larger than the other cutout.
7) Small acrylic cutout was placed on top of the large acrylic cutout.

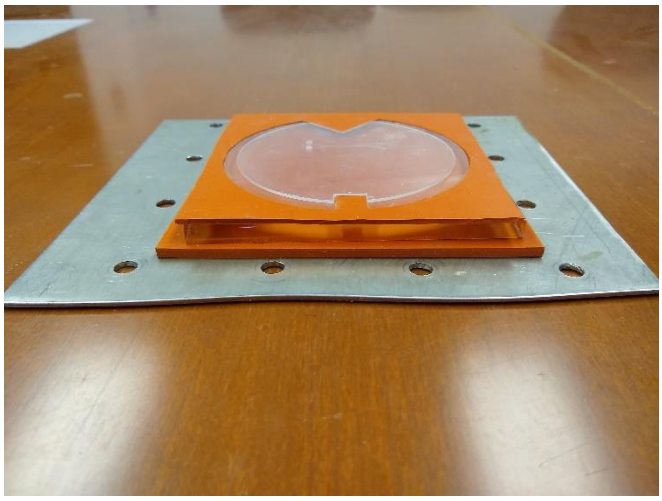

Figure 35. Assembly until placing the cutouts

8) Glass plate was placed over the small acrylic.

9) Silicone rubber was placed on the glass plate.

10) A steel plate was placed on the silicone rubber. Bolts were used for positioning.

11) Two aluminium bars were clamped to the steel plates.

12) Torque was applied on the clamps.

13) Bolts were removed because it was observed that bolts do not contribute to the pressure when the bars are actuated.

The optimal combination was found at 2.5 hours exposure to 100° C temperature with 0.3 Nm torque on the clamps. For this combination, no air-bubbles were found and preliminary observations of the flow channel under the microscope showed negligible deformations. Figure 37 shows the bonded acrylics. Four more acrylic cutouts were bonded using this combination out of which three had no air bubbles. Hence, this combination was finalized for further requirements.

Figure 36. Complete assembly

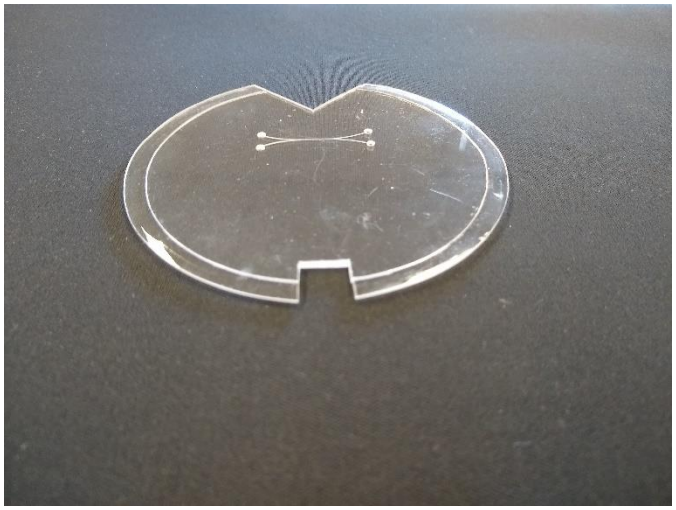

Figure 37. Bonded acylics

4.4) Gluing inlet outlet tubes and soldering

The next step consisted of gluing the inlet and outlet tubes to the inlet and outlet ports respectively. PVC tubes were glued to the inlet and outlet ports by using superglue. A copper wire was used for positioning as shown in figure 38.

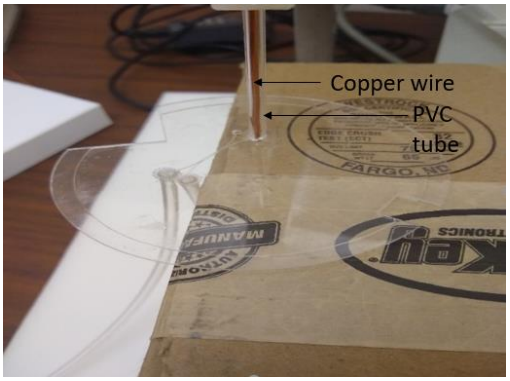

Figure 38. Attaching inlets and outlets

Attaching the transducer

The transducer was cut into required dimensions and bonded to the acrylic device by using two-part marine grade epoxy. The resin and hardener were mixed in the ratio of 2:1 and degassed in avacuum chamber for 15 minutes. A 3D printed back support for the transducer was used to hold the transducer against the acrylic.

4.5) Complete device

The completed device is shown in figure 39. As seen in the figure, there were no air bubbles in the acrylic and the transducer is well bonded. In addition, soldering was properly performed on the space available on the transducer. Before testing the device with cell-microbubble conjugates, information about a few aspects of the device was required in order to determine the device's suitability for testing.

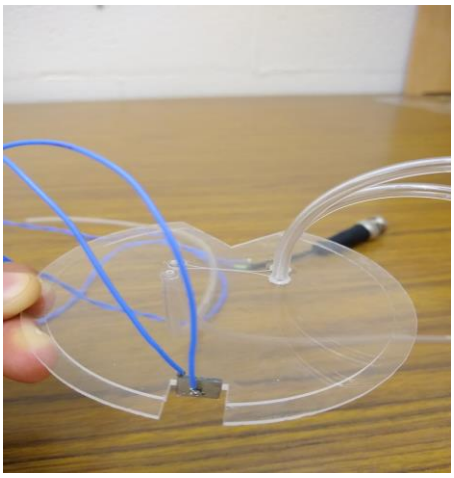

Figure 39. Complete device

Chapter 5. Characterization of the device

As mentioned in chapter 4, the next step after simulation and fabrication was characterizing the device, i.e determining the suitability for testing. For this purpose, it was necessary to obtain information about possibility of open circuits or short circuits, flow channel blockages, and coupling of the transducer to the device. Three experiments were performed for obtaining this information.

5.1) Electrical impedance analysis

In a qualitative sense, the electrical impedance signifies the opposition that a circuit presents to a current when a voltage is applied. Quantitatively speaking, electrical impedance is the ratio of complex voltage to complex current. Hence, the magnitude of electrical impedance is ratio of magnitudes of complex voltage and complex current, and the phase of electrical impedance is the difference in phases of complex voltage and complex current at a specific frequency. When the impedance reaches its minimum value when varied against frequency, the transducer vibrates most readily and most efficiently converts the electrical energy input into mechanical energy. This is the resonance frequency of the transducer [69].

The aim of this experiment was to determine the resonance frequency of the transducer attached to the device. Although the resonance frequency of the transducer was 2 MHz as mentioned in the chapter 2, it shifts due to the mass loading on the device. It was essential to find the resonance frequency of the device to operate at maximum efficiency.

The device was connected to an impedance analyzer by using a BNC cable and impedance curves were generated. Figure 40 shows the impedance curve. Magnitude and phase of the impedance were plotted and the resonance frequency was calculated by the software. The resonance

frequencies were 2.15 MHz and 2.20 MHz. We conclude that it is advisable to change the driving frequency to 2.15 or 2.2 MHz in further simulations for better energy conversion efficiency. It was also concluded that there are no shorts or open circuits since the generation of impedance curves implies faultless electrical circuit.

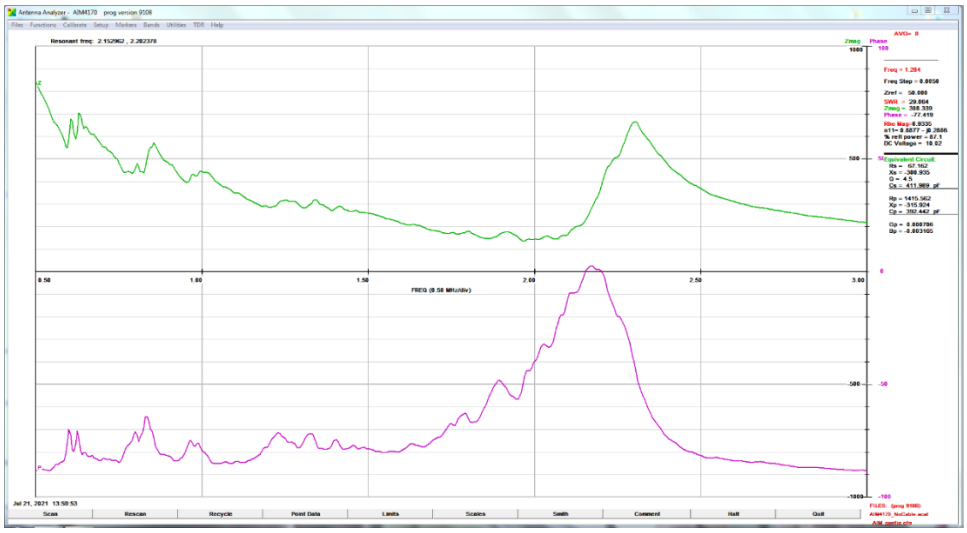

Figure 40. Electrical impedance analysis

5.2) Flow continuity in the flow channel

This experiment aimed to investigate any blockages in the flow channel and verify that the sheath flow and sample flow do not mix. Water was used as sheath fluid, and a green dye solution represented the sample flow. As shown in figure 41, the device was mounted on an experimental setup with a 10x magnification microscope focused on the center of the flow channel. Syringes were loaded on the syringe pumps and connected to the inlet and outlet ports. The experiment was performed at a flow rate of 0.05 ml/hr for both sheath and sample flow. This flow rate was determined based on the previous iteration of the device. Data from microbubble experiments on the previous device suggested that increasing the flow rate above 0.05 ml/hr reduced the visibility of microbubbles. Lower flow rates than 0.05 ml/hr would slow down the sorting process.

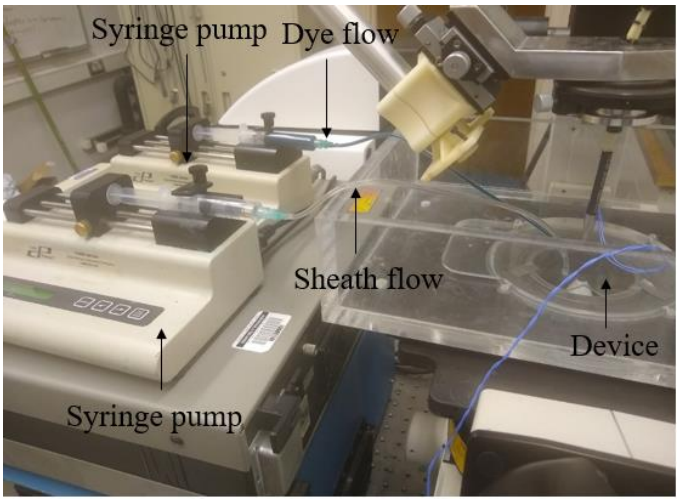

Figure 41. Experimental setup for flow continuity experiment

We observed smooth flow from the inlets tubes to outlet tubes indicating that there were no blockages in the flow channel and that the geometry led to smooth laminar flow of both the sheath liquid and sample liquid. Figure 42 shows the image of the flow channel under the microscope. We can clearly see that the green dye solution does not mix with the water for 0.05 ml/hr. This implied that the cell-microbubble mixture would also not mix with the sheath flow, which was necessary for the cell sorting process as mentioned in chapter 2.

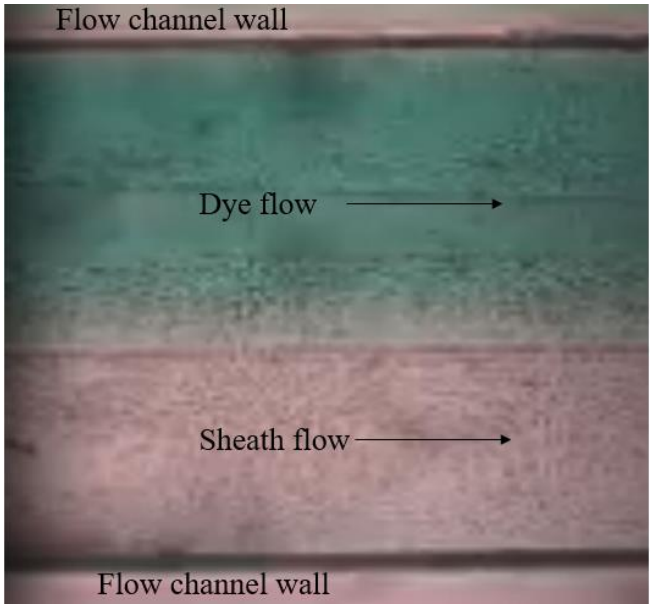

Figure 42. Image of the flow channel under the microscope. Turbulent mixing of the solutions does not occur

5.3) Pulse-echo

Initial studies with pushing microbubbles in the flow channel were inconclusive. Sometimes they responded to the ultrasound pulse, while other times they seemed not to respond. We needed a method to determine if the acoustic waves were reaching the flow channel. Unfortunately, the channel was inaccessible to a hydrophone. We thus decided to try a pulse-echo method to detect reflected waves from the channel.

The principle of pulse-echo is as follows. A short ultrasonic pulse is sent into a test material by a transducer. The pulsed wave reflects from imperfections in the test material and is received by the same transducer. The received pulsed waves are converted to an electrical signal with the amplitude representing the intensity of the reflection and the distance representing the arrival time of the reflection.

The experimental setup is illustrated in figure 43. The device was connected to a pulser-receiver (Panametrics Model 5072PR), which generates a single pulse and detects the reflected signal. The pulser-receiver was connected to an oscilloscope for displaying the received signal.

Ideally, an echo would be observed with the flow channel filled with air. However, the received signals were too noisy and it was difficult to differentiate the echo spike corresponding to the flow channel from the noise floor. To overcome this issue, we used the fact that acoustic impedance of acrylic plastic is closer to acoustic impedance of water than that of air. Hence, there would be negligible reflections from the water filled channel and considerable reflections from the air-filled flow channel since echo intensity increases with impedance mismatch.

To execute this, a pulse was introduced to the transducer and the receive signal data was recorded from the oscilloscope for both air-filled and water filled flow channel. The signals were subtracted and plotted against time (Figure 44). With this setup, we can clearly see a spike at 43 microseconds, proving that the ultrasound is getting transmitted into the device and reaching the flow channel.

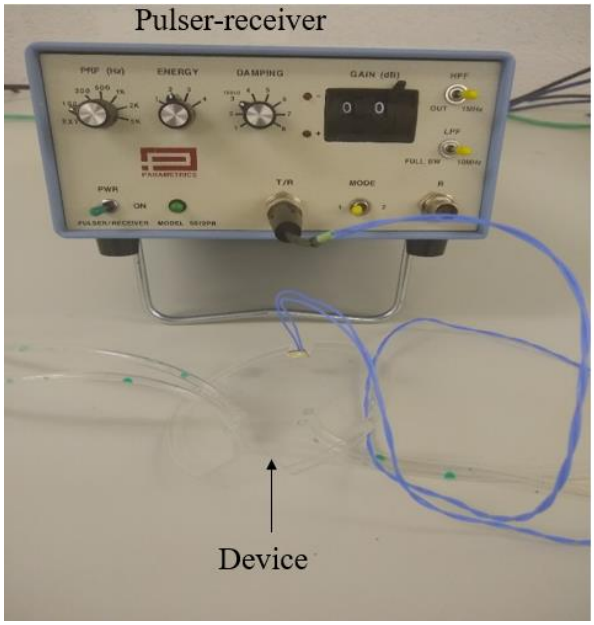

Figure 43. Pulse-echo experiment

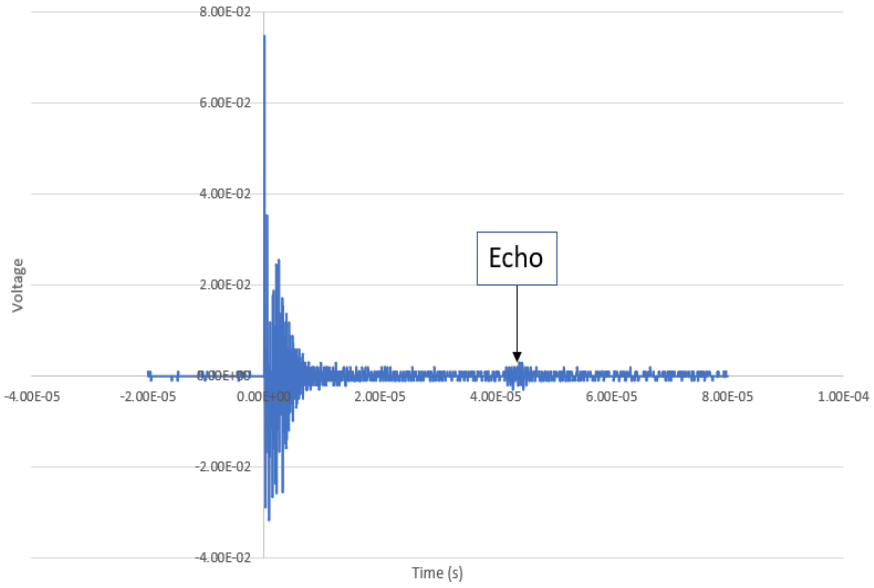

Figure 44. Difference of received signals of air-filled and water-filled flow channel. The echo spike is seen at 43 microseconds

To summarize, from the data described in this section, we found that the resonance frequency of the system increased slightly from 2 to 2.15 MHz or 2.2 MHz. We also found that the channel dimensions and overall functionality was good, as the sheath and sample flows were smooth, laminar, and resulted in no observable mixing. We also showed that some energy is arriving at the channel, but we still have work to do to determine whether the waves are shear or longitudinal

Chapter 6. Summary and future work

The thesis aimed at designing, fabricating, and characterizing a microfluidic device for Microbubble cell sorting (MiCS). This work was the next step after proving the feasibility of MiCS. The device was designed by applying various design considerations and FEA simulations. A critical design parameter was the distance between flow channel and the transducer, which was optimized to place the flow channel in the acoustic far-field. The device was fabricated successfully using manufacturing processes like laser cutting, micromachining, acrylic bonding, and soldering. Major challenges encountered while fabricating the device were optimization of parameters for acrylic bonding and avoiding tool breakage during machining. The device was characterized by performing experiments including impedance analysis, pulse-echo testing and examining the flow continuity in the flow channel.

Future work will primarily involve performing experiments with microbubbles and then cell-microbubble conjugates. Preliminary experiments were performed using poly dispersed microbubbles. Since the simulations were performed for frequency domain, continuous wave was employed in the experiments, but caused overheating of the transducer. This can be overcome by using a pulsed wave. More information on the effect of pulsed waves on the pressure field in the flow channel can be obtained by performing time-domain simulations. In general, the simulations can capture more aspects of reality, like increased height of the transducer, mass of soldering filler material, inclusion of epoxy layer between transducer and acrylic cutouts.

References

1. Takahashi, K., et al., Induction of pluripotent stem cells from adult human fibroblasts by defined factors. Cell, 2007. 131(5): p. 861-72.

2. Takahashi, K., et al., Induction of pluripotent stem cells from mouse embryonic and adult fibroblast cultures by defined factors. Cell, 2006. 126(4): p. 663-76.

3. Pitcher, C.J., et al., HIV-1-specific CD4+ T cells are detectable in most individuals with active HIV-1 infection, but decline with prolonged viral suppression. Nat Med, 1999. 5(5): p. 518-25.

4. Brenchley, J.M., et al., T-cell subsets that harbor human immunodeficiency virus (HIV) in vivo: implications for HIV pathogenesis. J Virol, 2004. 78(3): p. 1160-8.

5. Szaniszlo, P., et al., Getting the right cells to the array: Gene expression microarray analysis of cell mixtures and sorted cells. Cytometry A, 2004. 59(2): p. 191-202.

6. Matt, P., et al., Biomarker discovery: proteome fractionation and separation in biological samples. Physiol Genomics, 2008. 33(1): p. 12-7.

7. Gomase, V.S., et al., Proteomics: technologies for protein analysis. Curr Drug Metab, 2008. 9(3): p. 213-20.

8. Altelaar, A.F., et al., Trends in ultrasensitive proteomics. Curr Opin Chem Biol, 2012. 16(1-2): p. 206-13.

9. Amos, P.J., et al., Methods of cell purification: a critical juncture for laboratory research and translational science. Cells Tissues Organs, 2012. 195(1-2): p. 26-40.

10. Tomlinson, M.J., et al., Cell separation: Terminology and practical considerations. J Tissue Eng, 2013. 4: p. 2041731412472690.

11. Shapiro, H.M., Practical flow cytometry. 4th ed. 2003, New York: Wiley-Liss. l, 681 p.

12. Snow, C., Flow cytometer electronics. Cytometry A, 2004. 57(2): p. 63-9.

13. Miltenyi, S., et al., High-Gradient Magnetic Cell-Separation with MACS. Cytometry, 1990. 11(2): p. 231-238.

14. Chalmers, J.J., et al., Flow through, immunomagnetic cell separation. Biotechnology Progress, 1998. 14(1): p. 141-148.

15. Yellen, B.B., et al., Traveling wave magnetophoresis for high resolution chip based separations. Lab Chip, 2007. 7(12): p. 1681-8.

16. Pamme, N., et al., On-chip free-flow magnetophoresis: Separation and detection of mixtures of magnetic particles in continuous flow. Journal of Magnetism and Magnetic Materials, 2006. 307(2): p. 237-244.

17. Pamme, N. et al., On-chip free-flow magnetophoresis: continuous flow separation of magnetic particles and agglomerates. Anal Chem, 2004. 76(24): p. 7250-6.

18. Liu, C.X., et al., On-chip separation of magnetic particles with different magnetophoretic mobilities. Journal of Applied Physics, 2007. 101(2).

19. Adams, J.D., et al., Multitarget magnetic activated cell sorter. Proc Natl Acad Sci U S A, 2008. 105(47): p. 18165-70.

20. Antfolk, M., et al., Continuous flow microfluidic separation and processing of rare cells and bioparticles found in blood - A review. Anal Chim Acta, 2017. 965: p. 9-35.

21. Antfolk, M., et al., Acoustofluidic, label-free separation and simultaneous concentration of rare tumor cells from white blood cells. Analytical Chemistry, 2015. 87(18): p. 9322-9328.

22. Cushing, K.W., et al., Elastomeric negative acoustic contrast particles for affinity capture assays. Anal Chem, 2013. 85(4): p. 2208-15.

23. Faridi, M.A., et al., MicroBubble activated acoustic cell sorting. Biomed Microdevices, 2017. 19(2): p. 23-30.

24. Goddard, G. et al., Ultrasonic particle concentration in a line-driven cylindrical tube. Journal of the Acoustical Society of America, 2005. 117(6): p. 3440-3447.

25. Gossett, D.R., et al., Label-free cell separation and sorting in microfluidic systems. Anal Bioanal Chem, 2010. 397(8): p. 3249-67.

26. Grenvall, C., et al., Two-dimensional acoustic particle focusing enables sheathless chip Coulter counter with planar electrode configuration. Lab Chip, 2014. 14(24): p. 4629-37.

27. Hartono, D., et al., On-chip measurements of cell compressibility via acoustic radiation. Lab on a Chip, 2011. 11(23): p. 4072-4080.

28. Jakobsson, O., et al., Continuous flow two-dimensional acoustic orientation of nonspherical cells. Anal Chem, 2014. 86(12): p. 6111-4.

29. Kaduchak, G. et al., Application of acoustic radiation pressure to align cells in a commercial flow cytometer. Proceedings of Meetings on Acoustics, 2013. 19(1): p. 045014.

30. Kim, S.H., et al., Highly efficient single cell arraying by integrating acoustophoretic cell pre-concentration and dielectrophoretic cell trapping. Lab Chip, 2015. 15(22): p. 4356-63.

31. Laurell, T., et al., Chip integrated strategies for acoustic separation and manipulation of cells and particles. Chemical Society Reviews, 2007. 36(3): p. 492-506.

32. Lenshof, A., et al., Acoustic whole blood plasmapheresis chip for prostate specific antigen microarray diagnostics. Anal Chem, 2009. 81(15): p. 6030-7.

33. Petersson, F., et al., Free flow acoustophoresis: microfluidic-based mode of particle and cell separation. Anal Chem, 2007. 79(14): p. 5117-23.

34. Petersson, F., et al., Separation of lipids from blood utilizing ultrasonic standing waves in microfluidic channels. Analyst, 2004. 129(10): p. 938-943.

35. Schmid, L., et al., Sorting drops and cells with acoustics: acoustic microfluidic fluorescence-activated cell sorter. Lab on a Chip, 2014. 14(19): p. 3710-3718.

36. Shields, C.W.t., et al., Elastomeric negative acoustic contrast particles for capture, acoustophoretic transport, and confinement of cells in microfluidic systems. Langmuir, 2014. 30(14): p. 3923-7.

37. Coakley, W.T., Ultrasonic separations in analytical biotechnology. Trends in Biotechnology, 1997. 15(12): p. 506-511.

38. Coakley, W.T., et al., Cell Manipulation in Ultrasonic Standing Wave Fields. Journal of Chemical Technology and Biotechnology, 1989. 44(1): p. 43-62.

39. Hsu, C.H., et al. Isolating cells from blood using buoyancy activated cell sorting (BACS) with glass microbubbles. in 14th International Conference on Miniaturized Systems for Chemistry and Life Sciences. 2010. Groningen, The Netherlands: Chemical and Biological Microsystems Society.

40. Matula, T.J., et al., Ultrasound-based cell sorting with microbubbles: A feasibility study. J Acoust Soc Am, 2018. 144(1): p. 41.

41. Bjerknes, V., Fields of force. 1906, New York,: The Columbia university press; etc. 2 p.

42. Chalmers, J.J., et al., Theoretical analysis of cell separation based on cell surface marker density. Biotechnol Bioeng, 1998. 59(1): p. 10-20.

43. Chalmers, J.J., et al., Quantification of cellular properties from external fields and resulting induced velocity: magnetic susceptibility. Biotechnol Bioeng, 1999. 64(5): p. 519-26.

44. Bomsztyk, K., et al., PIXUL-ChIP: integrated high-throughput sample preparation and analytical platform for epigenetic studies. Nucleic Acids Res, 2019. 47(12): p. e69.

45. van der Meer, S.M., et al., Microbubble spectroscopy of ultrasound contrast agents. J Acoust Soc Am, 2007. 121(1): p. 648-56.

46. Zhao, H., et al., A spectral boundary integral method for flowing blood cells. J. Comp. Phys., 2010. 229: p. 3726–2744.

47. Freund, J.B. et al., Transport of particles by magnetic forces and cellular blood flow in a model microvessel. Phys. Fluids, 2012. 24: p. 051904.

48. Isfahani, A.H.G. et al., Forces on a wall-bound leukocyte in a small vessel due to red cells in the blood stream. Biophysical Journal, 2012. 103: p. 1604–1615.

49. Freund, J.B., The flow of red blood cells through a narrow spleen-like slit. Phys. Fluids, 2013. 25: p. 110807.

50. Freund, J.B. et al., The wall-stress footprint of blood cells flowing in microvessels. Biophysical Journal, 2014. 106(3): p. 752-762.

51. Bryngelson, S.H. et al., Global stability of flowing red blood cell trains. Phys. Rev. Fluids, 2018. 7(3): p. 085007.

52. Boselli, F., et al., Hemodynamic shear stress patterns predict the orientation of convergent tissue movements in the embryonic heart. Development, 2017. 144(23): p. 4322–4327.

53. Krehbiel, J.D., et al., Algal cell disruption using microbubbles to localize ultrasonic energy. Bioresource Technology, 2014. 173: p. 448–451.

54. Krehbiel, J.D. et al., Stokes flow inside a sphere in an inviscid extensional flow. Zeitschrift fu¨r angewandte Mathematik und Physik (ZAMP), 2017. 68(81): p. 1-13.

55. Freund, J.B., Suppression of shocked-bubble expansion due to tissue confinement with application to shock-wave lithotripsy. J. Acoustical Soc. America, 2008. 123(5): p. 2867–2874.

56. Movahed, P., et al., Ultrasound-induced bubble clusters in tissue-mimicking agar phantoms. Ultrasound in Med. Biol., 2017. 43(10): p. 2318–2328.

57. Movahed, P., et al., Cavitation-induced damage of soft materials by focused ultrasound bursts: A fracture- based bubble dynamics model. J. Acoust. Soc. Am., 2016. 140(2): p. 1374–1386.

58. Jurg D., et al., Piezoelectricity and application in the excitation of acoustic fields for ultrasonic particle manipulation. Lab Chip, 2012, 12, 506

59. George M. W. et al. Patterning cells and their environments using multiple laminar fluid flows in capillary networks.

60. https://doc.comsol.com/5.5/doc/com.comsol.help.aco/aco_ug_pressure.05.002.html

61. https://doc.comsol.com/5.5/doc/com.comsol.help.sme/sme_ug_solid.07.02.html

62. https://doc.comsol.com/5.5/doc/com.comsol.help.acdc/acdc_ug_electric_fields.07.002.html

63. https://doc.comsol.com/5.6/doc/com.comsol.help.aco/aco_ug_acousticstructure.07.04.html

64. https://doc.comsol.com/5.5/doc/com.comsol.help.aco/aco_ug_multiphysics_couplings.13.03.html

65. https://doc.comsol.com/5.5/doc/com.comsol.help.aco/aco_ug_pressure.05.106.html

66. M N Afsar., Precision Millimeter-Wave Measurements of Complex Refractive Index, Complex Dielectric Permittivity, and Loss Tangent of Common Polymers

67. Xuelin Z., et al Study of PMMA thermal bonding. Microsyst Technol (2007) 13: 403–407

68. https://www.trumpf.com/en_GB/solutions/applications/laser-cutting/

69. https://www.americanpiezo.com/knowledge-center/piezo-theory/determining-resonance-frequency.html

Appendix

A1) Discussion on machining parameters

This section mentions some important points that were considered while machining the flow channel, as well as the reasons for selecting the parameters mentioned in table 9. The width of the inlet and outlet sections of the flow channel was 0.0137 inches. Hence, the available size lower than 0.0137 inches was selected as the diameter of the end-mill bit. A major problem faced while machining was breakage of the end-mill bit due to high stresses. Possible reasons included overheating, high feed rate, high RPM, and/or collection of acrylic dust in the machining area. A coolant was used to avoid overheating. The RPM was lowered to 2000 RPM from 2500 RPM which significantly increased the bit life. A similar reasoning was applied for feed rate, which was reduced to 0.5 inches/min from 1 inch/min. The depth of cut is another important factor in tool breakage. High depth of cut increases the shear stresses due to increased contact of the end-mill bit with acrylic. Hence, the total depth of the flow channel was cut in six equal passes, thereby reducing the contact of end-mill bit with acrylic for each pass. These changes in the machining parameters enabled long bit life.

Figure below shows the geometry of the flow channel as viewed from the top. The blue circle represents the end-mill bit. A detailed G-code is provided later. As mentioned in the previous section, the machining was done in six equal passes. Two important factors were considered while deciding the machine tool path. The first factor was that the end-mill bit should be in continuous contact with the acrylic for each pass, to ensure smooth surface finish. The second factor was that the end-mill bit should not travel against the points where the flow channel arms join (points B and C), to avoid breakage of acrylic at those points.

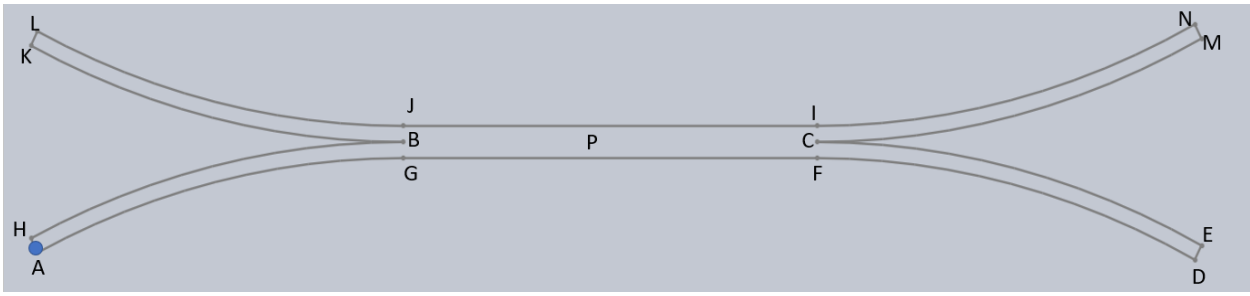

The G-code used for machining is provided. The origin is shown in the figure below. Top surface of acrylic was (z=0)

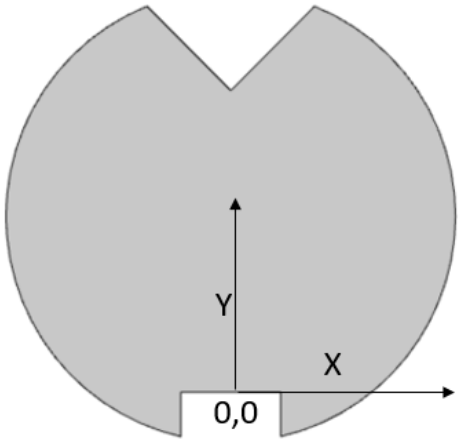

%holes

%diameter .013inch

%First pass

g0 z.1

g0 x-0.554512352 y1.652185581

g1 z-0.001 f0.5 %straight

g2 x-0.147637795 y1.765153543 r0.757105491 %clockwise

g1 x0.147637795 y1.765153543 %straight

g2 x0.554512352 y1.652185581 r0.757105491 %clockwise

g1 x0.55491186 y1.652854951 %straight

g3 x0.147637795 y1.764374016 r0.816506702 %anticlockwise

g1 x-0.147637795 y1.764374016 %straight

```
g3 x-0.55491186 y1.652854951 r0.816506702          %anticlockwise
g2 x-0.147637795 y1.764374016 r0.816506702         %clockwise
g1 x0.147637795 y1.778933071                       %straight
g1 x-0.147637795 y1.778933071                      %straight
g2 x-0.55491186 y1.890452135 r0.816506702          %clockwise
g1 x-0.554512352 y1.891121506                      %straight
g3 x-0.147637795 y1.778153543 r0.757105491         %anticlockwise
g1 x0.012598 y1.778153543                          %straight
g1 x0.147637795 y1.778933071                       %straight
g3 x0.55491186 y1.890452135 r0.816506702           %anticlockwise
g1 x0.554512352 y1.891121506                       %straight
g2 x0.147637795 y1.778153543 r0.757105491          %clockwise
g1 x-0.0126 y1.778153543                           %straight
g0 z.1

%Second pass
g0 z.1
g0 x-0.554512352 y1.652185581
g1 z-0.002 f0.5                                    %straight
g2 x-0.147637795 y1.765153543 r0.757105491         %clockwise
g1 x0.147637795 y1.765153543                       %straight
g2 x0.554512352 y1.652185581 r0.757105491          %clockwise
g1 x0.55491186 y1.652854951                        %straight
g3 x0.147637795 y1.764374016 r0.816506702          %anticlockwise
g1 x-0.147637795 y1.764374016                      %straight
g3 x-0.55491186 y1.652854951 r0.816506702          %anticlockwise
g2 x-0.147637795 y1.764374016 r0.816506702         %clockwise
g1 x0.147637795 y1.778933071                       %straight
```

```
g1 x-0.147637795 y1.778933071                    %straight
g2 x-0.55491186 y1.890452135 r0.816506702        %clockwise
g1 x-0.554512352 y1.891121506                    %straight
g3 x-0.147637795 y1.778153543 r0.757105491       %anticlockwise
g1 x0.012598 y1.778153543                        %straight
g1 x0.147637795 y1.778933071                     %straight
g3 x0.55491186 y1.890452135 r0.816506702         %anticlockwise
g1 x0.554512352 y1.891121506                     %straight
g2 x0.147637795 y1.778153543 r0.757105491        %clockwise
g1 x-0.0126 y1.778153543                         %straight
g0 z.1

%Third pass
g0 z.1
g0 x-0.554512352 y1.652185581
g1 z-0.003 f0.5                                  %straight
g2 x-0.147637795 y1.765153543 r0.757105491       %clockwise
g1 x0.147637795 y1.765153543                     %straight
g2 x0.554512352 y1.652185581 r0.757105491        %clockwise
g1 x0.55491186 y1.652854951                      %straight
g3 x0.147637795 y1.764374016 r0.816506702        %anticlockwise
g1 x-0.147637795 y1.764374016                    %straight
g3 x-0.55491186 y1.652854951 r0.816506702        %anticlockwise
g2 x-0.147637795 y1.764374016 r0.816506702       %clockwise
g1 x0.147637795 y1.778933071                     %straight
g1 x-0.147637795 y1.778933071                    %straight
g2 x-0.55491186 y1.890452135 r0.816506702        %clockwise
g1 x-0.554512352 y1.891121506                    %straight
```

g3 x-0.147637795 y1.778153543 r0.757105491 %anticlockwise

g1 x0.012598 y1.778153543 %straight

g1 x0.147637795 y1.778933071 %straight

g3 x0.55491186 y1.890452135 r0.816506702 %anticlockwise

g1 x0.554512352 y1.891121506 %straight

g2 x0.147637795 y1.778153543 r0.757105491 %clockwise

g1 x-0.0126 y1.778153543 %straight

g0 z.1

%Fourth pass

g0 z.1

g0 x-0.554512352 y1.652185581

g1 z-0.004 f0.5 %straight

g2 x-0.147637795 y1.765153543 r0.757105491 %clockwise

g1 x0.147637795 y1.765153543 %straight

g2 x0.554512352 y1.652185581 r0.757105491 %clockwise

g1 x0.55491186 y1.652854951 %straight

g3 x0.147637795 y1.764374016 r0.816506702 %anticlockwise

g1 x-0.147637795 y1.764374016 %straight

g3 x-0.55491186 y1.652854951 r0.816506702 %anticlockwise

g2 x-0.147637795 y1.764374016 r0.816506702 %clockwise

g1 x0.147637795 y1.778933071 %straight

g1 x-0.147637795 y1.778933071 %straight

g2 x-0.55491186 y1.890452135 r0.816506702 %clockwise

g1 x-0.554512352 y1.891121506 %straight

g3 x-0.147637795 y1.778153543 r0.757105491 %anticlockwise

g1 x0.012598 y1.778153543 %straight

```
g1 x0.147637795 y1.778933071                    %straight
g3 x0.55491186 y1.890452135 r0.816506702        %anticlockwise
g1 x0.554512352 y1.891121506                    %straight
g2 x0.147637795 y1.778153543 r0.757105491       %clockwise
g1 x-0.0126 y1.778153543                        %straight
g0 z.1

%Fifth pass
g0 z.1
g0 x-0.554512352 y1.652185581
g1 z-0.005 f0.5                                 %straight
g2 x-0.147637795 y1.765153543 r0.757105491      %clockwise
g1 x0.147637795 y1.765153543                    %straight
g2 x0.554512352 y1.652185581 r0.757105491       %clockwise
g1 x0.55491186 y1.652854951                     %straight
g3 x0.147637795 y1.764374016 r0.816506702       %anticlockwise
g1 x-0.147637795 y1.764374016                   %straight
g3 x-0.55491186 y1.652854951 r0.816506702       %anticlockwise
g2 x-0.147637795 y1.764374016 r0.816506702      %clockwise
g1 x0.147637795 y1.778933071                    %straight
g1 x-0.147637795 y1.778933071                   %straight
g2 x-0.55491186 y1.890452135 r0.816506702       %clockwise
g1 x-0.554512352 y1.891121506                   %straight
g3 x-0.147637795 y1.778153543 r0.757105491      %anticlockwise
g1 x0.012598 y1.778153543                       %straight
g1 x0.147637795 y1.778933071                    %straight
g3 x0.55491186 y1.890452135 r0.816506702        %anticlockwise
g1 x0.554512352 y1.891121506                    %straight
```

```
g2 x0.147637795 y1.778153543 r0.757105491        %clockwise
g1 x-0.0126 y1.778153543                         %straight
g0 z.1

%Sixth pass
g0 z.1
g0 x-0.554512352 y1.652185581
g1 z-0.006 f0.5                                  %straight
g2 x-0.147637795 y1.765153543 r0.757105491       %clockwise
g1 x0.147637795 y1.765153543                     %straight
g2 x0.554512352 y1.652185581 r0.757105491        %clockwise
g1 x0.55491186 y1.652854951                      %straight
g3 x0.147637795 y1.764374016 r0.816506702        %anticlockwise
g1 x-0.147637795 y1.764374016                    %straight
g3 x-0.55491186 y1.652854951 r0.816506702        %anticlockwise
g2 x-0.147637795 y1.764374016 r0.816506702       %clockwise
g1 x0.147637795 y1.778933071                     %straight
g1 x-0.147637795 y1.778933071                    %straight
g2 x-0.55491186 y1.890452135 r0.816506702        %clockwise
g1 x-0.554512352 y1.891121506                    %straight
g3 x-0.147637795 y1.778153543 r0.757105491       %anticlockwise
g1 x0.012598 y1.778153543                        %straight
g1 x0.147637795 y1.778933071                     %straight
g3 x0.55491186 y1.890452135 r0.816506702         %anticlockwise
g1 x0.554512352 y1.891121506                     %straight
g2 x0.147637795 y1.778153543 r0.757105491        %clockwise
g1 x-0.0126 y1.778153543                         %straight
g0 z.1
```

A2) ζ field

The images provided below consist of ζ fields in the flow channel for simulation 1. As reported in the simulation section, solutions were obtained for various combinations of height, width and distance of the flow channel. Height and width of the flow channel are displayed below. Only the image of the flow channel for each simulation is shown. When ζ is 1, it signifies forward traveling waves in the at that point, and -1 signifies backward traveling wave and 0 signifies standing wave. Forward traveling wave was desired. Following are the images of only the flow channel for all the combinations.

The color scale of ζ is represented below

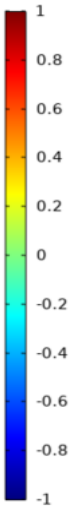

ζ fields for distance of the flow channel from the transducer=20mm

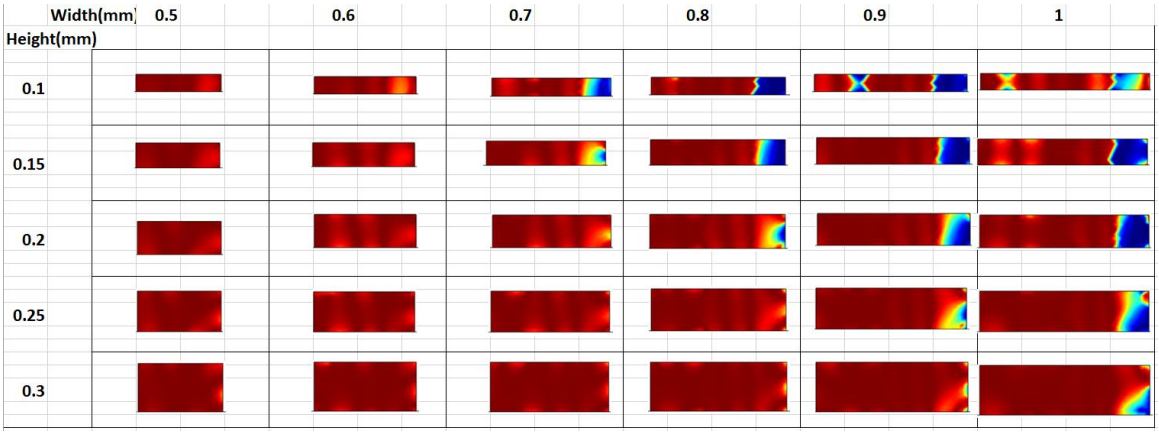

ζ fields for distance of the flow channel from the transducer=25mm

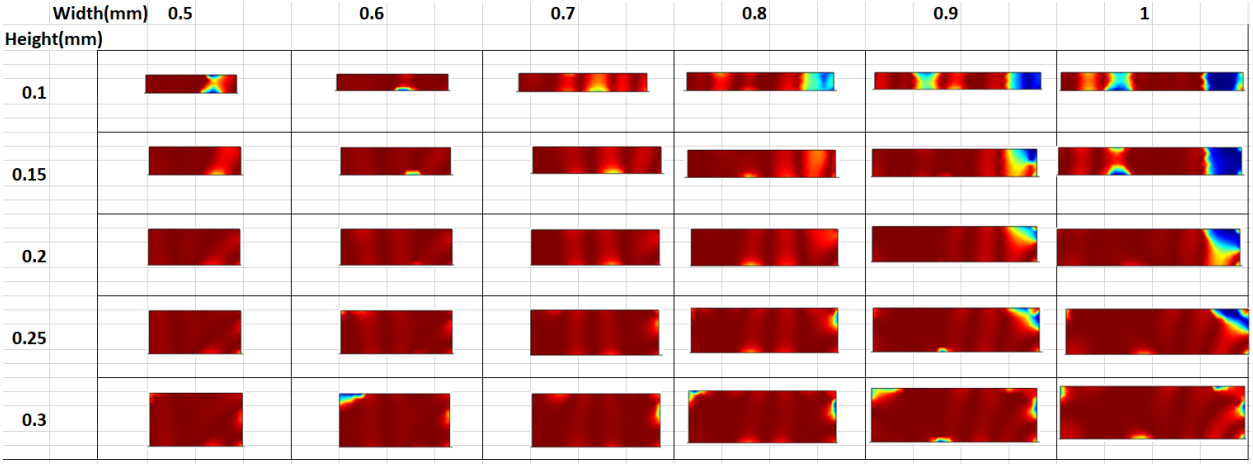

ζ fields for distance of the flow channel from the transducer=30mm

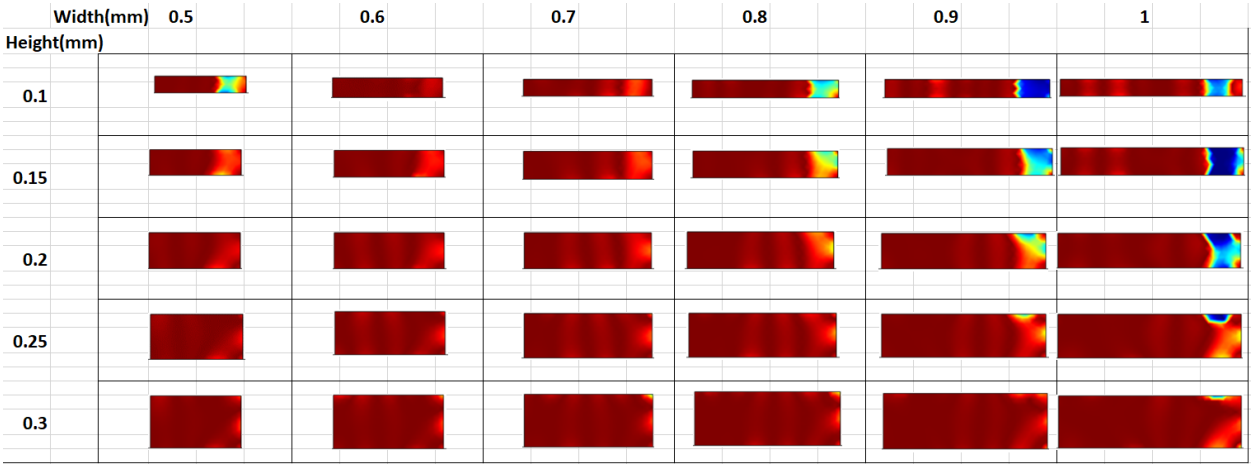

ζ fields for distance of the flow channel from the transducer=35mm

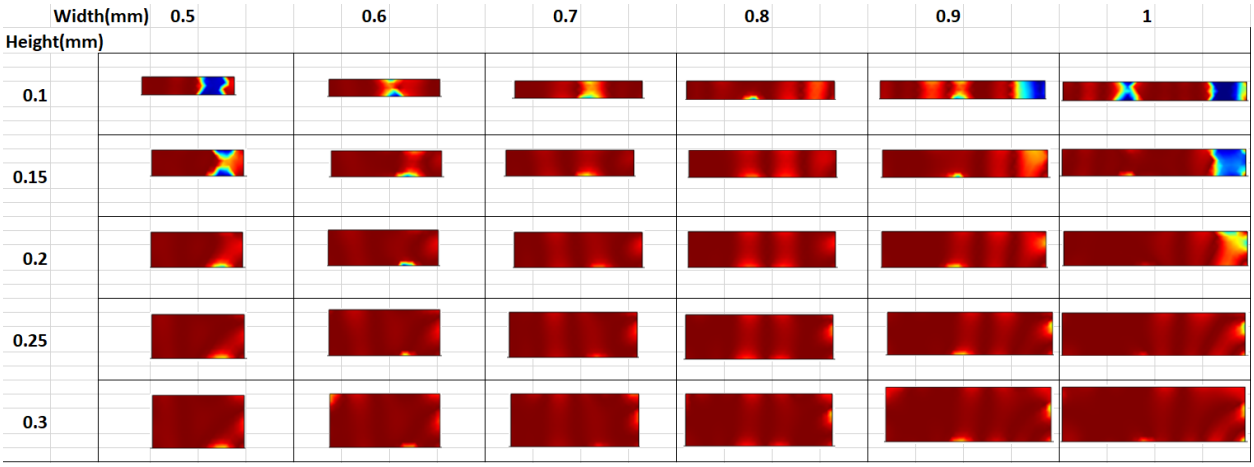

ζ fields for distance of the flow channel from the transducer=40 mm

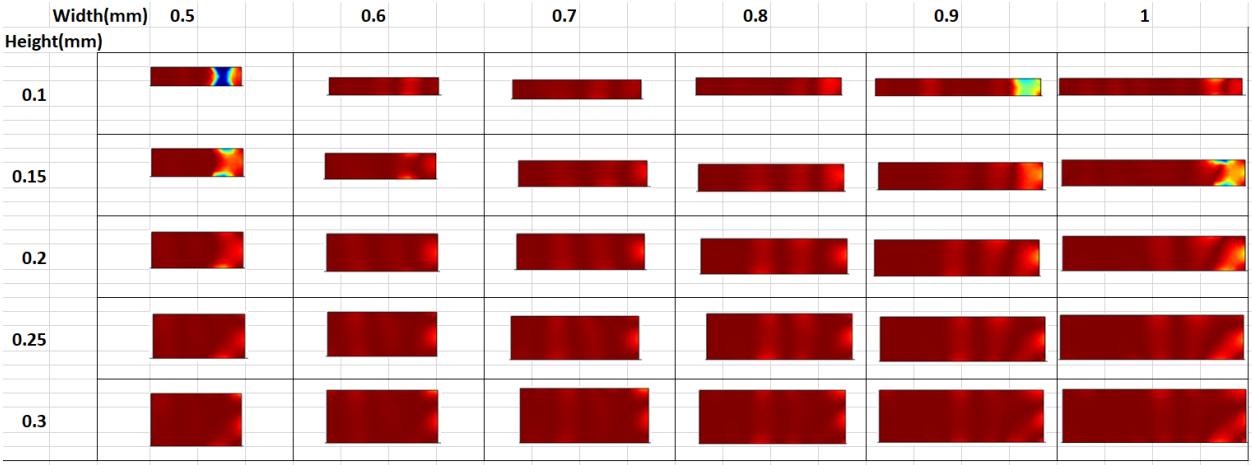

ζ fields for distance of the flow channel from the transducer=45 mm

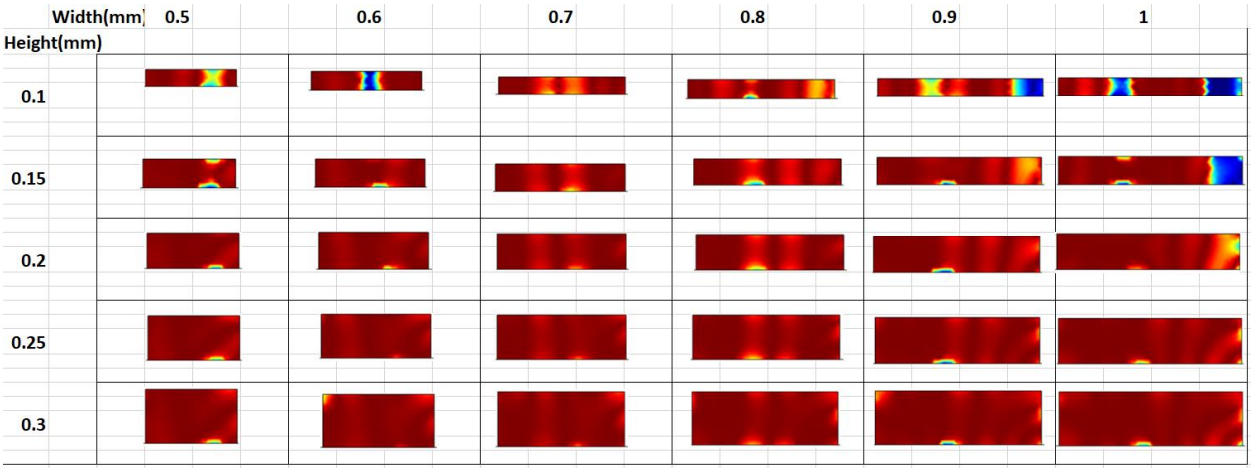

ζ fields for distance of the flow channel from the transducer=50mm